AGU ADVANCING EARTH AND SPACE SCIENCE

Water Resources Research

RESEARCH ARTICLE
10.1029/2020WR028775

Numerical and Analytical Modeling of Flow Partitioning in Partially Saturated Fracture Networks

Jannes Kordilla[1], **Marco Dentz**[2], **and Alexandre M. Tartakovsky**[3,4]

[1]University of Goettingen, Geoscientific Centre, Goettingen, Germany, [2]Institute of Environmental Assessment and Water Research (IDAEA), Spanish National Research Council (CSIC), Barcelona, Spain, [3]Department of Civil and Environmental Engineering, University of Illinois Urbana-Champaign, Urbana, IL, USA, [4]Pacific Northwest National Laboratory, Richland, WA, USA

Key Points:

- Horizontal fractures control dispersion during infiltration events within vertical preferential pathway
- Partitioning dynamics at intersections control uptake and release from subvertical fractures
- An analytical solution is derived and the dynamics upscaled via convolution to obtain nondimensional characteristics

Correspondence to:
J. Kordilla,
jkordil@gwdg.de

Citation:
Kordilla, J., Dentz, M., & Tartakovsky, A. M. (2021). Numerical and analytical modeling of flow partitioning in partially saturated fracture networks. *Water Resources Research*, *57*, e2020WR028775. https://doi.org/10.1029/2020WR028775

Received 10 SEP 2020
Accepted 2 FEB 2021

Abstract Infiltration processes in fractured-porous media remain a crucial, yet not very well understood component of recharge and vulnerability assessment. Under partially saturated condition flows in fractures, percolating fracture networks and fault zones contribute to the fastest spectrum of infiltration velocities via preferential pathways. Specifically, the partitioning dynamics at fracture intersections determine the magnitude of flow fragmentation into vertical and horizontal components, hence the bulk flow velocity and dispersion of fracture networks. Here we derive an approximate analytical solution for the partitioning process and validate it using smoothed particle hydrodynamics simulations. The transfer function is conceptually based on simulation results and laboratory experiments carried out in previous works. It allows efficient flow simulation through fracture networks with simple cubic structures and an arbitrary number of fractures and aperture sizes via linear response theory and convolution of a given input signal. We derive a nondimensional bulk flow velocity ($\tilde{v}$) and dispersion coefficient ($\tilde{D}$) to characterize fracture networks in terms of dimensionless horizontal and vertical time scales τ_m and τ_0. The dispersion coefficient strongly depends on the horizontal time scale and converges toward a constant value of 0.08 within reasonable fluid and geometrical parameter ranges, while the nondimensional velocity exhibits a characteristic $\tilde{v} \sim \tau_m^{-1/2}$ scaling. Given that hydraulic information is often only available at limited places within (fractured-porous) aquifer systems (boreholes or springs), our study intends to provide an analytical concept to potentially reconstruct internal fracture network geometries from external boundary information, such as the dispersive properties of discharge (groundwater level fluctuations).

1. Introduction

Estimation of infiltration and recharge remains one of the most important challenges in modern hydrogeology (Scanlon & Cook, 2002; Scanlon et al., 2006) and is directly related to important topics such as integrated water resources management (Alkhatib et al., 2019; Engelhardt et al., 2013), safety of nuclear waste repositories (Bodvarsson et al., 1997; Tsang et al., 2015), and storage, release and degradation of nitrate and other agrochemical products (Ascott et al., 2016, 2017; Kurtzman et al., 2013; Wang et al., 2013). In contrast to the long-prevailing opinion that fractures (or, generally speaking, highly permeable heterogeneities embedded in porous media) do not transmit water under nonequilibrium conditions due to the strong capillary forces in the adjacent matrix (Singhal & Gupta, 2010), arrival times recorded in field and laboratory experiments strongly suggest the existence of rapid preferential flow along fractures, fracture networks, and fault zones (Dahan et al., 2000; Weisbrod et al., 2000; Zhou et al., 2006). The dynamic activation of preferential flow domains within the vadose zone controls the short- and long-term hydraulic response of the groundwater to precipitation signals (Nimmo & Perkins, 2018) and therefore affects the magnitude and temporal distribution of recharge. This is even more critical given the current predictions of climate-change-induced erratic and potentially extreme precipitation patterns (Black, 2009) that require precise estimation and management of limited recharge volumes, especially in systems with thick vadose zones (Dvory et al., 2016; El-Hakim & Bakalowicz, 2007).

Despite the importance of the vadose zone for infiltration processes both with respect to volumetric extent and share of the total aquifer volume, modeling approaches often do not (and can not due to missing information) consider the complexity of fractured-porous media to model the delay in arrival times and

therefore dispersion of an input signal. The complexity arises from geological heterogeneities that provide continuous pathways on various scales for rapid percolation and transport within fractures. In karst systems, precipitation is commonly partitioned into diffuse and preferential components, where the latter is commonly linked to direct infiltration in the surrounding area of surface depressions, dry valleys, and dolines (Gunn, 1981; Kordilla et al., 2012; Sauter, 1992; Williams, 2008). Fault zones may cut across several geological units and provide catchment-scale preferential flow paths in the form of strongly connected clusters of fractures (Bodvarsson et al., 1997; Flint et al., 2001; H. H. Liu et al., 2004). Tectonically induced stress fields and stress field changes generally promote the formation of local discontinuities, such as fractures, joints, and fault zones in consolidated porous rocks (Ford & Williams, 2013; Neslon, 2001). What sets such features apart from typical pore space geometries is their strong anisotropic character, that is, their length or spatial extent is orders of magnitude larger than their aperture. When fractures are connected, they can form percolating clusters (Adler et al., 2013; Berkowitz & Scher, 1995) that can reach length scales far beyond the thickness of individual geological layers/units and potentially extend across the entire vadose zone. Similar features can be observed in soil systems, a type of material where the heterogeneity is commonly associated with macropores (wormholes), which can also form percolating clusters (Hussain et al., 2019; Jarvis, 1998; Nimmo, 2010).

Assessing recharge dynamics in fractured-porous systems on the field scale is difficult (Scanlon & Cook, 2002). Phreatic zone techniques assess recharge at the water table or at springs (e.g., tracers, water table fluctuations; Cook & Solomon, 1997; Nimmo & Perkins, 2018). Therefore, the estimates can potentially reflect catchment-scale dynamics or at least subcatchment recharge processes within the hydraulic influence area of the measurement point. In contrast, vadose zone techniques rely on measurements above the groundwater table (e.g., lysimeters, Darcy's law, tracers, Chambers et al., 2019; Heppner et al., 2007; Rossman et al., 2014). They allow a rather localized quantification of recharge or water content and only integrate a limited volume above the point of measurement as infiltration commonly occurs nearly vertical. Because most of these methods rely on simple assumptions about internal systems geometry and percolation processes, the predictive power and temporal resolution is often limited (Scanlon & Cook, 2002).

To shed light on complex infiltration processes, laboratory-scale experiments have been a promising addition to the former investigation methods because they allow important processes to be isolated under well-controlled conditions that are often impossible to observe in situ. Small-scale laboratory experiments for gravity-driven partially saturated flow often exhibit erratic or chaotic flow dynamics (Dragila & Weisbrod, 2004; Nicholl & Glass, 2005; Su et al., 2001; T. Wood & Huang, 2015). In general, flow modes on the wall of wide fractures evolve with increasing flow rates from thin adsorbed films to droplets and rivulets to wavy surface films (Dippenaar & Van Rooy, 2016; Dragila & Wheatcraft, 2001; Ghezzehei, 2004; Jones et al., 2017). Different flow modes may also coexist. Consequently, experimental results are difficult to cast into meaningful frameworks. This especially concerns the complex flow dynamics at fracture intersections, which act as critical relay points controlling: (1) the overall connectivity of fracture networks (Adler et al., 2013); (2) the flow partitioning dynamics between connected fracture elements (Dragila & Weisbrod, 2004; Xue et al., 2020; Yang et al., 2019); and, ultimately, (3) the distribution of flow modes on fracture surfaces (Dippenaar & Van Rooy, 2016; Jones et al., 2017; Shigorina et al., 2019), which, in turn, can affect the interaction between the porous matrix and fracture (Tokunaga, 2009; Tokunaga & Wan, 1997). Here, the term "partitioning" refers to the process of fluid redistribution at a fracture intersection, which depends on the relation between capillary, inertial, and viscous forces (Nicholl & Glass, 2005) and complexities such as velocity-dependent contact angles (Xue et al., 2020; Yang et al., 2019).

In terms of fracture aperture, numerical and laboratory studies of unsaturated flow in fractures have covered various length scales, from submillimeter scales (Glass et al., 2003; Ji et al, 2004, 2006; Nicholl & Glass, 2005) over ranges close to the capillary-inertial transition around 0.7 mm (T. R. Wood et al., 2002, 2005) to apertures well within the inertial-dominated regime (Dragila & Weisbrod, 2004; Tartakovsky & Meakin, 2005a, 2005b; Tokunaga & Wan, 1997, 2001; Huang et al., 2005; M. Liu et al., 2007). Studies of free surface flow on a fracture plane without an intersection have been conducted by Shigorina et al. (2019); Kordilla et al. (2013); Hayden et al. (2012) and Ghezzehei (2004).

Depending on the experimental setup, studies have focused either on the partitioning process at fracture intersections (Dragila & Weisbrod, 2004) or the (long-term) bulk system response (Ebel & Nimmo, 2013; Nimmo, 2010), both of which are integral parts of understanding preferential flow dynamics through fractured systems. For the former case, a single fracture intersection of a horizontal and a vertical fracture is often "constructed," for example, by breaking glass plates, which results in a quasi-two-dimensional setup (Ji et al., 2006). Modifications to this setup include experiments with a slight offset at the fracture intersection or T-shaped intersections at various degrees of rotation (T. R. Wood et al., 2005; Xue et al., 2020; Yang et al., 2019). Intersections resembling an inverted Y-structure have been studied by Dragila and Weisbrod (2004), M. Liu et al. (2007) and Tartakovsky and Meakin (2005a). The combination of several commonly cross-shaped fracture intersections allows flow convergence to be studied, that is, the deviation from classical volume-effective diffusive flow dynamics that are typical for nonfracture porous media. Studies of this kind have been conducted by T. R. Wood et al. (2002, 2005); T. Wood and Huang (2015); Glass et al. (2003); LaViolette et al. (2003), often reaching timescales of several minutes or days. In the study by Glass et al. (2003), fractures are embedded into an impermeable matrix, while the other authors constructed their fracture networks from geological materials. Incorporation of the porous matrix can be considered another important classification parameter of fracture-scale studies. For large-aperture fractures, that is, inertial-dominated flow systems that limit the contact time between fracture flow, matrix flow, and/or a low-permeable matrix, the effect of matrix storage may be neglected. This can be observed in fractured karst systems, where fractures are often enlarged by dissolution (Benson, 2001; Dijk et al., 2002) or fractured crystalline rocks with extremely low matrix porosity and a severely limited advective potential.

Despite these research efforts, the gap between small-scale process understanding and larger-scale application is still significant. In our recent work (Noffz et al., 2019), we demonstrated how to model breakthrough behavior in terms of discharge at the bottom of arbitrary long stacks of sugar-cube fracture arrays (Barenblatt et al., 1960) via linear response theory and convolution of input signals, whereas the transfer function has been obtained empirically for a given setup of a wide-aperture vertical surface intersected by a horizontal one. However, it is desirable to obtain the form of the transfer function a priori using information about the internal geometry as well as fluid properties and fluid–solid interaction characteristics. Therefore, in this work, we provide an analytical solution for the transfer function and validate it using numerical simulations. The analytical solution describes the horizontal fracture infiltration until critical pressure thresholds trigger the breakthrough. The following dynamics are governed by Washburn-type flows and are conceptually based on the numerical studies and former laboratory studies (Noffz et al., 2019). Vertical flows are approximated by a film flow model. Finally, we employ linear response theory to model flow through arbitrary numbers of fracture intersections with explicit geometry and derive nondimensional dispersion and velocity parameters ($\tilde{D}, \tilde{v}$) that depend on the dimensionless horizontal and vertical fracture time scales (τ_m, τ_0). Flows are shown to converge to a near-constant dispersion coefficient with increasing τ_m, while nondimensional velocities scale as $\tilde{v} \sim \tau_m^{-1/2}$ within feasible critical Reynolds number ranges.

2. SPH Model

We use a two-dimensional SPH model to analyze complex flow partitioning at fracture intersections. SPH is a Lagrangian meshless method able to simulate complex flows with highly dynamic interfaces and is especially suited for the simulation of free-surface (pseudo-multiphase) liquid flows with a continuous gas phase, effects of surface tension, and static/dynamic contact angles. We use a two-dimensional version of the massively parallel three-dimensional code of Kordilla et al. (2017) that has been extended with an alternative formulation of the no-slip boundary condition. For a detailed description of the SPH free flow model and its implementation in a parallel code, the reader is referred to Kordilla et al. (2017) and references therein. The SPH equations are summarized in Appendix A.

Here, we validate the SPH code for two classical static and dynamic flow cases that are related to the processes encountered in our application of flow in fractures, Poiseuille flow in a parallel plate system, and capillary rise in a vertical tube. The Poiseuille flow example serves to verify the proper implementation of viscous forces at the solid–fluid interface. These forces are important for both the film flow, where flow is bounded on one side only, and the flow that fully fills horizontal fractures.

2.1. Poiseuille Flow

In this section, we demonstrate that for sufficiently large values of the friction coefficient β in the SPH momentum conservation Equations A3 and A6, the SPH method recovers the solution of the NS equations subject to no-slip boundary conditions at the fluid–solid boundary. Specifically, we use the SPH code with β ranging from 1×10^{-1} to 1×10^{2} kgm^{2}s^{-1} to simulate a two-dimensional Poiseuille flow problem and validate the SPH solutions for velocity against the analytical solution for the no-slip boundary condition (Sigalotti et al., 2003)

$$v_x(y,t) = \frac{a_f}{2\nu}(y^2 - d^2) + \sum_0^\infty \frac{16(-1)^n d^2 a_f}{\nu\pi^3(2n+1)^3}\cos\left[\frac{(2n+1)\pi y}{2d}\right]\exp\left[-\frac{(2n+1)^2\pi^2\nu t}{4d^2}\right], \tag{1}$$

where the center is located at $y = 0$, $d = L/2$ such that the solid boundaries are located at $y = \pm d$, $\nu = \mu/\rho$ is the kinematic viscosity, and a_f is the component of the body force per unit mass acting in the x direction (the direction of flow).

Flow is simulated using the following parameter set: the interparticle spacing is $\Delta x = 5 \times 10^{-5}$ m, $L = 200\Delta x = 1 \times 10^{-2}$ m, $\rho = 1{,}000$ kgm^{-3}, and $\mu = 1.25 \times 10^{-3}$ kgm^{-1}s^{-1} , and an acceleration of $a_f = 1.25 \times 10^{-5} ms^{-2}$ is applied parallel to the x direction. Five layers of boundary particles are placed at $y = 0$ and $y = L$ to assure kernel consistency. For the given parameter set, this yields a Reynolds number of $\mathrm{Re} = \frac{v_x^\infty L\rho}{\mu} = 1.0$, where v_x^∞ is the maximum steady-state velocity.

Results indicate that the SPH solution converges to the exact no-slip solution for $\beta > 10$ (which corresponds to the artificial slip length $\lambda < L/100$) with an error on the order of 1.5% or lower. This holds for all time steps during the initial acceleration of the fluid within the capillary. It should be noted that for much higher values of β, the time steps have to become increasingly smaller according to Equation A7, which was not enforced in these simulations. Therefore, a slight increase in the error can be observed for values above $\beta = 20$, a strategy that is employed in this study.

2.2. Capillary Rise in a Tube

Here we simulate capillary rise in tubes of varying radii and compare the equilibrium fluid column height to the classical theory of Jurin (1718) and the extended theories of Legait and de Gennes (1984) and Barozzi and Angeli (2014).

The classical theory of capillary rise is based on the parallel plate concept:

$$\frac{dh}{dt} = \frac{\Delta P}{h(t)}\frac{(2r)^2}{12\mu} \tag{2}$$

where r is the radius of the fracture, and h is the height of the triple contact line from the water surface. The total pressure in a two-dimensional system consists of the capillary pressure and the pressure due to the weight of the water column

$$P_c^{2D} = \frac{\sigma cos(\theta_0)}{r} \qquad P_h = \rho g h(t) \tag{3}$$

Plugging the total pressure $\Delta P = \Delta P_c^{2D} - P_h$ into Equation 2 and for $dh/dt = 0$, the maximum rise becomes:

$$\Delta h = \frac{\sigma cos(\theta_0)}{r\rho g} \tag{4}$$

Because the curvature of the meniscus slightly depends on h, a common extension of Equation 4 is given by Legait & de Gennes (1984) as:

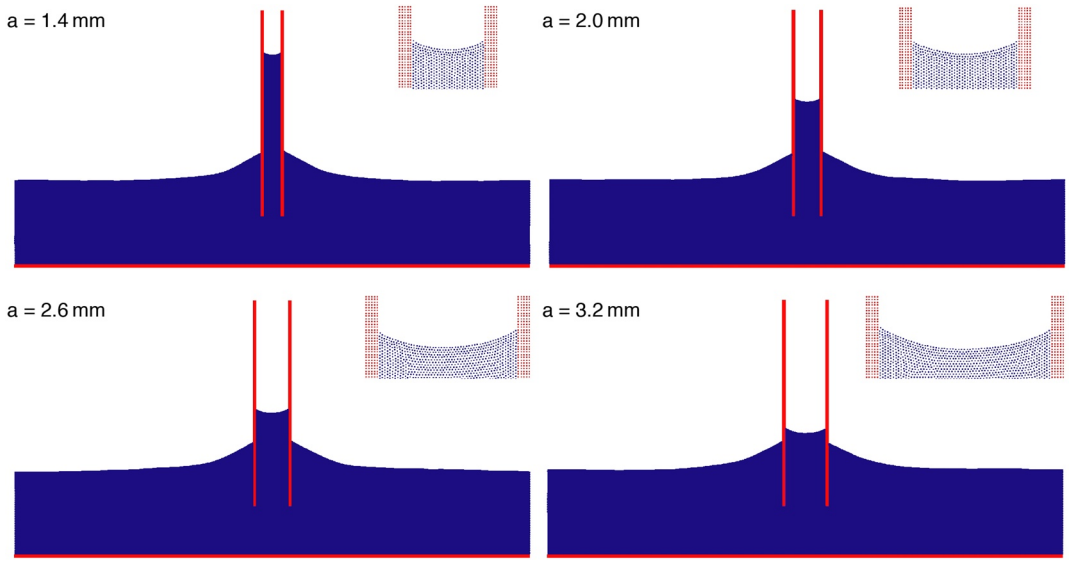

Figure 1. 2D simulations of capillary rise shown at steady-state conditions. The insets show the upper fluid front. The height of the capillary is $L_c = 1.7$ cm, and the width of the domain is $L_w = 4.0$ cm with periodic boundary conditions in the x-direction.

$$\Delta h = \frac{1 - \kappa^2 r^2 0.175}{\kappa^2 r} \qquad \kappa = \left(\frac{\rho g}{\sigma cos(\theta_0)} \right)^{1/2} \tag{5}$$

Barozzi and Angeli (2014) extend the solution by adding a correction term that accounts for the additional fluid volume over the apex of the meniscus

$$\Delta h = \frac{\sigma cos(\theta_0)}{r \rho g} - \frac{r}{3cos(\theta)} \tag{6}$$

The SPH simulations are run with an interparticle spacing of $\Delta x = 5 \times 10^{-5}$ m, and a density of $\rho = 1{,}000$ kgm^{-3} and a body force of $g = 9.81$ ms^{-2} are applied in normal direction to the bottom boundary. The viscosity is $\mu = 0.001$ kgm^{-1}s^{-1} and the no-slip condition is enforced with $\beta = 25$. The speed of sound is set to $c_0 = 3$ m.s^{-1}. Interaction forces are set to $s_{sf} = 0.015$ and $s_{ff} = 0.02$, which yields a surface tension of $\sigma = 0.0742$ kgs^{-2} and a static contact angle of $\theta_0 = 69°$. The domain has a width of $L_x = 800\Delta x = 4.0$ cm. The height of the capillary is $L_y = 340\Delta x = 1.7$ cm and is placed $\Delta L_y = 60\Delta x = 3$ mm above the bottom boundary. Mirror boundaries are applied in the x-direction. All solid boundaries are five particles thick to assure kernel consistency. Simulations are initiated with a flat fluid surface covering the domain with an initial height of $145\Delta x = 7.25$ mm. The aperture of the capillary is varied in a range of 1.5–3.5 mm.

Simulations are run until an equilibrium is established and the maximum height is reached within the capillary. In order to measure Δh, we determine the minimum height $h_{\min}$ of the fluid as the average of the water height $20\Delta x$ away from the left and right mirror boundaries (see Figure 1). The maximum height $h_{\max}$ of the fluid column is measured at the outer part of the capillary meniscus, and we therefore obtain $\Delta h = h_{\max} - h_{\min}$. The contact angles at equilibrium are obtained from a circle fit using the Pratt method (Pratt, 1987) (Figure 2, left).

Results of the SPH simulations and theoretical results are shown in Figure 2. Numerical results are in good agreement with the theoretical predictions and lie in between the predictions of Jurin (1718), Legait and de Gennes (1984) and Barozzi and Angeli (2014). The latter study takes into account the effect of additional fluid volume above the meniscus apex which becomes increasingly important when the capillary rise h_c is on the order of capillary radius r. This is true for the shown example ($h_c/2r \sim 0.5$–2.2).

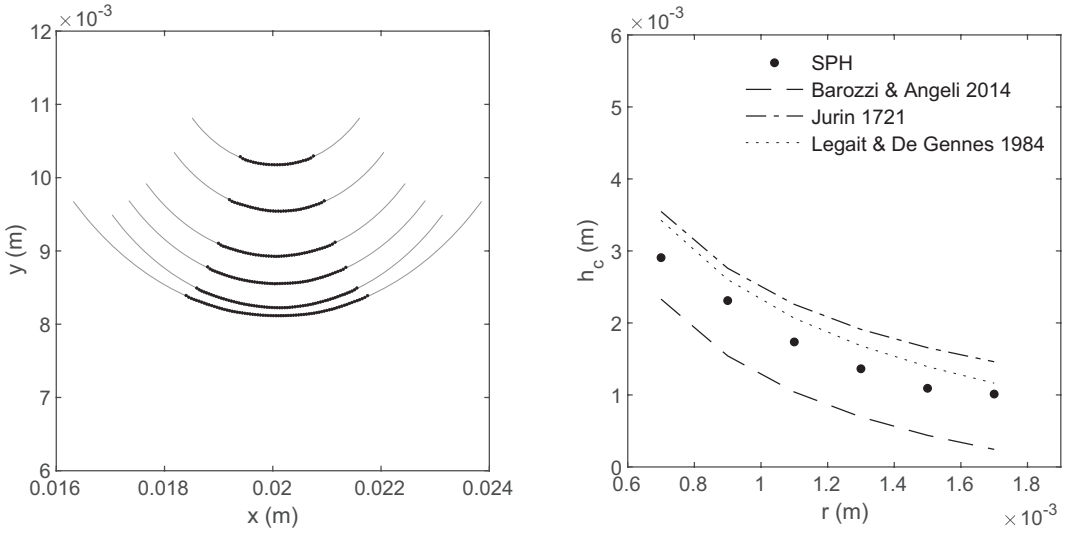

Figure 2. (Left) Liquid–gas interfaces for all capillary sizes and the respective circle fit using the Pratt method. (Right) Theoretical predictions of the capillary rise h_c are plotted using the average contact angle of all simulations.

3. Results and Discussion

In the following subsections we (1) conceptualize the flow partitioning at a T-type fracture intersection, (2) derive an analytical transfer function for the partitioning including fluid movement on the vertical surfaces, (3) provide an upscaling solution via convolution and linear response theory, and finally (4) derive expressions for arrival times and bulk dispersion that are then (5) analyzed in nondimensional form to provide a comprehensive picture of the larger-scale infiltration dynamics and its relation to the internal geometry.

3.1. Rivulet Flow Partitioning at a Fracture Intersection

In this section, we derive a solution for the partitioning dynamics of rivulet flow down a vertical plane intersected by a horizontal smooth fracture (see Figure 3) and compare it to our SPH model results. We consider the threshold at which critical capillary pressures within the horizontal fracture are high enough to route flow further down onto the vertical surface. At this point, flow in the horizontal fracture transitions from a linear plug-flow type into a Washburn-type flow regime. It should be noted that the conceptual model assumes that flow within the horizontal fracture is capillary-driven; therefore, wide-aperture horizontal fractures (e.g., cave-like structures) where the fluid may establish free-surface flows (low capillary flows) are not taken into account. Furthermore, we assume that flow on the vertical surfaces takes the shape of rivulets. This assumption is often made in soil systems for preferential flows (Bogner & Germann, 2019; Germann & Hensel, 2006; Nimmo, 2010) and has been shown to also hold under laboratory conditions (Noffz et al., 2019), yet, more complex flow-rate-dependent modes (droplet, slugs) may occur (Ghezzehei, 2004; Kordilla et al., 2017) that trigger early partitioning at intersections (T. R. Wood et al., 2005; Xue et al., 2020; Yang et al., 2019) and are different from the sequential approach considered in this work.

The flow rate $Q_h(t)$ (m^2s^{-1}) in the horizontal fracture is approximately given by the Darcy law:

$$Q_h(t) = \frac{ka(P_{in}(t) - P_f)}{\mu l(t)}, \tag{7}$$

where t is time from the moment water entered the horizontal fracture, $k = a^2/12$ (m^2), a is the aperture (m), μ is the viscosity, P_f and $P_{in}(t)$ are the pressures at the invading front (point 1 in Figure 3a) and the horizontal

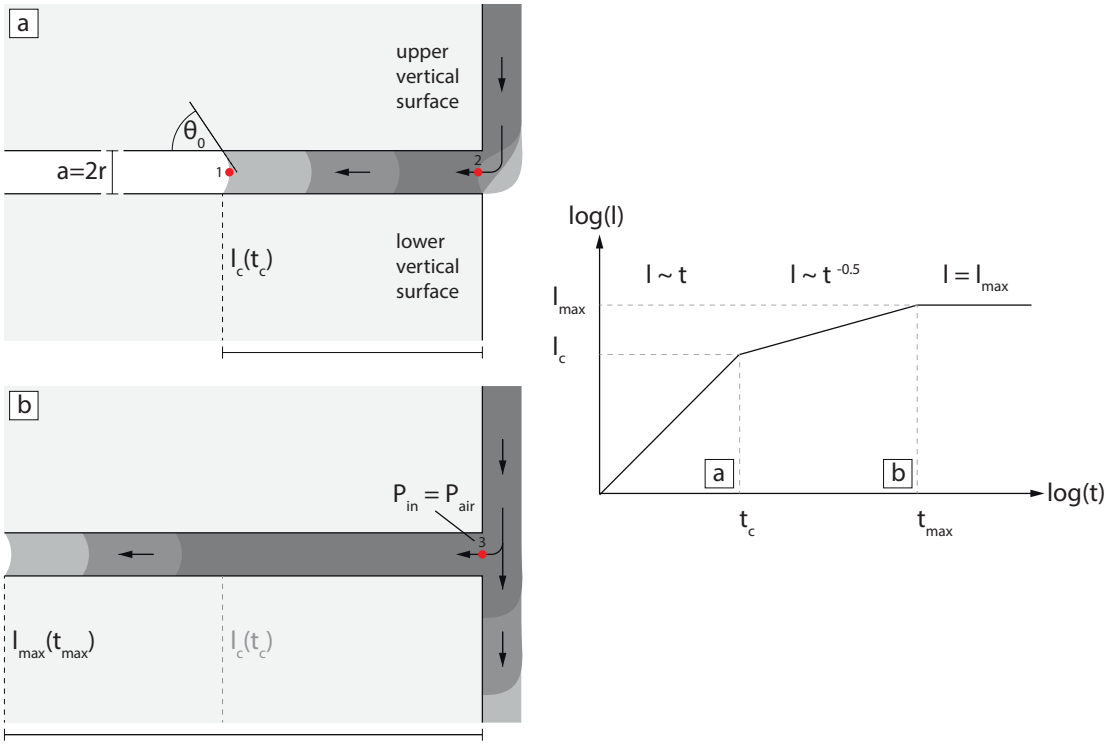

Figure 3. Conceptual model for the partitioning process at a fracture intersection. Flows on the vertical surfaces are bounded by one fracture wall only assuming wide aperture conditions. Breakthrough occurs at time t_c after which the horizontal imbibition scales as $l \sim t^{0.5}$.

fracture entrance (point 2 in Figure 3a), respectively, and $l(t)$ is the distance from the front to the fracture entrance.

From the Young-Laplace law, the pressure at the invading front is

$$P_f = P_{air} - \frac{\sigma}{R} = P_{air} - \sigma\frac{2\cos(\theta)}{a}, \tag{8}$$

where σ is the surface water–air surface tension, P_{air} is the air pressure, $R = \frac{a}{2\cos\theta}$ is the front curvature, and θ is the contact angle.

Initially, all flow in the vertical fracture is diverted to (imbibed into) the horizontal fracture, that is, $Q_h(t) = Q_0$, as shown in Figure 3a. Later, flow partitions, where flow both penetrates the horizontal fracture and flows down the wall of the vertical fracture segment, as depicted in Figure 3b. When flow is partitioned, $P_{\text{in}}(t) = P_{\text{air}}$ (point 3 in Figure 3b). In the following analysis, we assume that partitioning occurs instantaneously at time $t = t_c$. Then, Equation 7 can be rewritten as

$$Q_h(t) = \begin{cases} Q_0, & t \le t_c, \\ \dfrac{2k\sigma\cos(\theta)}{\mu l(t)}, & t > t_c. \end{cases} \tag{9}$$

The front position in the horizontal fracture at the time of partitioning is obtained by setting

$$Q_0 = \frac{2k\sigma\cos(\theta)}{\mu l_c}. \tag{10}$$

Thus, we obtain

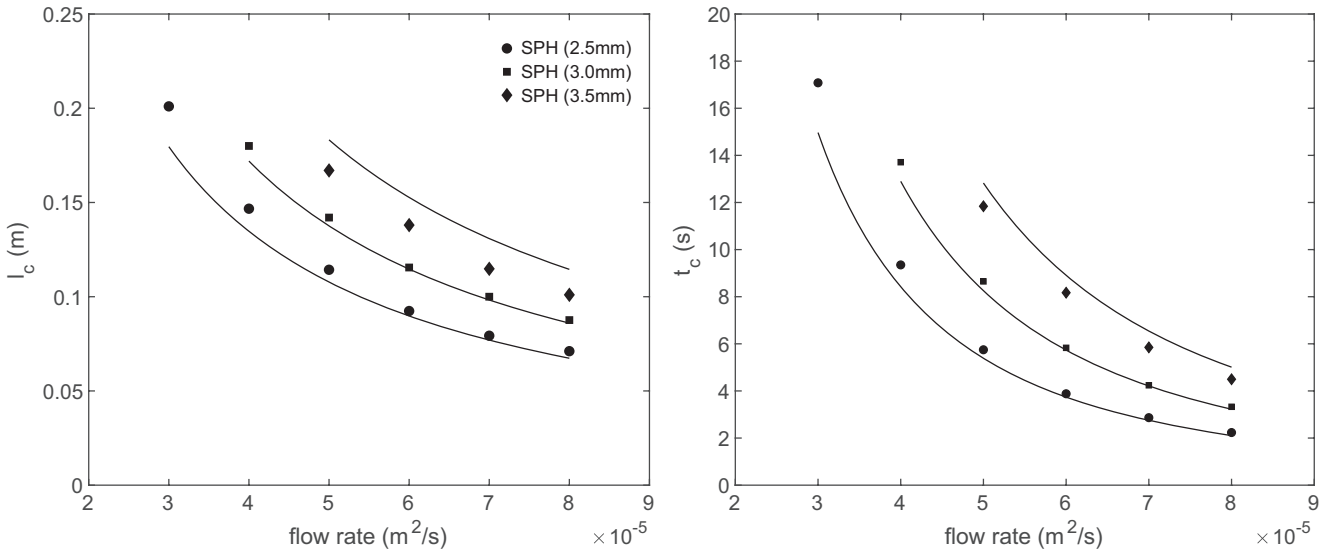

Figure 4. Critical transition times t_c and critical length l_c of the SPH model and the respective analytical solutions (black lines, Equations 11 and 12). Contact angles are taken as averages of the angle at initial fracture penetration and the angle at t_c.

$$l_c = \frac{2k\sigma\cos(\theta)}{\mu Q_0}. \tag{11}$$

The velocity of the displacing fluid for $t < t_c$ is equal to Q_0/a. At times t_c, the penetration depth is given by $Q_0 t_c/a = l_c$ and thus we obtain for t_c

$$t_c = \frac{l_c a}{Q_0} = \frac{2ka\sigma\cos(\theta)}{\mu Q_0^2}. \tag{12}$$

The penetration depth $l(t) \sim t$ increases linearly with time for $t < t_c$ and according to $l(t) \sim \sqrt{t}$ for $t > t_c$ (see Appendix B). The Washburn-type flow behavior is valid only at times much larger than t_c. We do not model the transitional flow behavior between the plug and Washburn modes, but represent the change between the two flow modes as abrupt. Thus, we approximate the penetration depth by matching the linear and square root behaviors at t_c as follows,

$$l(t) = \begin{cases} \dfrac{Q_0 t}{a}, & t \le t_c, \\ l_c\sqrt{t\,/\,t_c}, & t > t_c. \end{cases} \tag{13}$$

Figure 4 shows l_c and t_c, computed from Equations 11 and 12 and direct SPH simulations, as a function of the flow rate Q_{in} for three horizontal apertures (2.5, 3, and 3.5 mm). SPH simulations for the fracture aperture 2.5 mm and three different flow rates are shown in Figure 5. In SPH simulations, we use an interparticle spacing of $\Delta x = 5 \times 10^{-5}$ m, a density of $\rho = 1{,}000$ kgm^{-3}, and a body force of $g = 9.81$ ms^{-2} applied normal to the horizontal fracture plane. The surface tension is $\sigma = 0.0742$ kgs^{-2} with the interaction parameters $s_{ff} = 0.015$ and $s_{sf} = 0.0125$ and speed of sound $c_0 = 3$ ms^{-1}. The viscosity is slightly increased to $\mu = 0.005$ kgm^{-1}s^{-1} to limit the required length of the horizontal fracture (and hence computation time), which was set to $L = 0.25$ m. The no-slip boundary condition is enforced with $\beta = 25$ (see Figure 6). For the flow rates between $Q_0 = 3 \times 10^{-5}$ m^{2}s^{-1} and 8×10^{-5} m^{2}s^{-1} and fracture apertures between $a = 2.5$ and 3.5 mm, the critical penetration length can be observed within the chosen fracture length. To avoid erratic partitioning behavior at the fracture intersections (i.e., bypassing droplets), we initiate the simulations with a rivulet on the upper vertical surface, which is already in contact with the horizontal fracture aperture at the start of

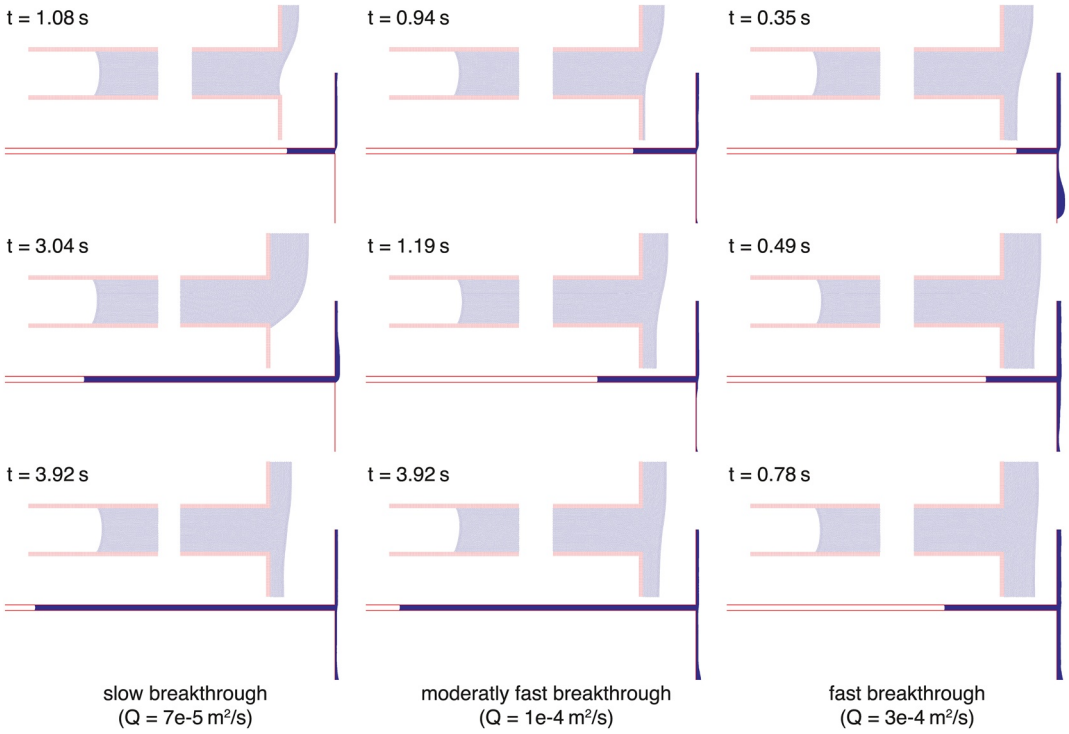

Figure 5. Breakthrough regimes at the horizontal fracture intersection (shown for an aperture of $a = 2.5$ mm) for three different flow rates (increasing from left to right) and at three time steps. Three regimes can be distinguished: (1) slow breakthrough, (2) moderately fast breakthrough, and (3) fast breakthrough. A detailed description of the regimes can be found in the text. The insets show the detailed view of the liquid–gas interface at the invading fluid front and at the fracture intersection.

the simulation. While under certain conditions this may prevent other partitioning patterns (e.g., droplets, snapping rivulets) at the intersection, Noffz et al. (2019) demonstrated with laboratory experiments that this behavior is to be expected at consecutive fracture intersections. Independent of the initial flow mode (rivulets, droplet), they found that after the first fracture intersection the flow on vertical walls was dom-

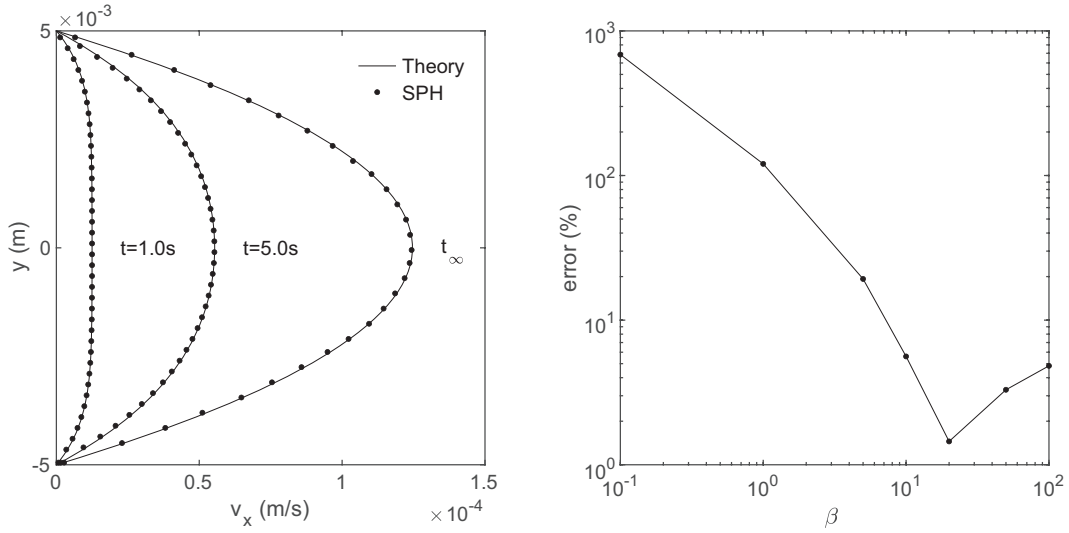

Figure 6. Comparison of the SPH model with the time-dependent solution for Poiseuille flow in a parallel plate system. The right figure shows the absolute percentage error, which is below ≈1.5% for sufficiently large β (>10), that is, proper no-slip conditions.

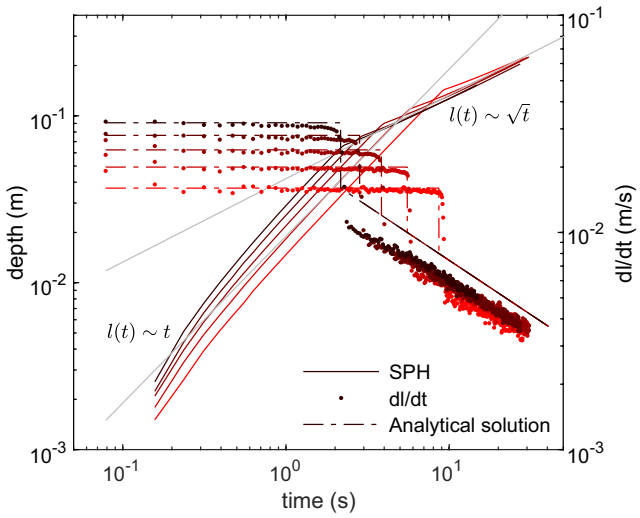

Figure 7. SPH simulations correctly recover the linear (plug-flow) and Washburn behavior. The inflow velocity dl/dt and the analytical solution (Equation 14) are in very good agreement. Note that the fluid front did not fully penetrate the horizontal fracture in the simulations; therefore, the cutoff at t_{max} (l = const., $dl/dt = 0$) is not visible here. Here, $a = 2.5$ mm and the inflow rate ranges from $Q_0 = 4 \times 10^{-5}$ m^{2}s^{-1} (bright red) to $Q_0 = 8 \times 10^{-5}$ (dark red). Gray lines indicate the two characteristic scaling regimes.

inated by rivulets. Figure 4 demonstrates that our SPH simulations are in good agreement with the analytical predictions of Equations 11 and 12 for small fracture apertures (2.5 and 3 mm) and larger Q_0 but slightly deviate for larger apertures (3.5 mm) and smaller Q_0, resulting in the maximum error of ~12%. We partially attribute this to the fact that the contact angle θ changes during the water penetration into the horizontal fracture (e.g., Popescu et al., 2008). In our analytical model, we disregard dynamic variations in the contact angle and compute θ as an average of the contact angles right after the onset of fracture penetration and close to t_c. Yet, Figure 4 demonstrates that our analytical solutions provide an overall good approximation of the partitioning dynamics.

3.2. Analytical Solution for the Transfer Function

We now derive analytical solutions for $l(t)$, the front position (or the depth of penetration) in the horizontal fracture, and $Q(t)$, which is the outflow rate below the horizontal fracture junction where fluid is discharged.

Given that the inflow consists of (1) a linear penetration phase and (2) a Washburn-type penetration period, we obtain an analytical solution as follows

$$\frac{dl}{dt} = v_f(t) = \frac{Q_0}{a}\begin{cases} 1, & t \le t_c, \\ \frac{1}{2}\left(\frac{t}{t_c}\right)^{-1/2}, & t_c < t < t_{max}. \end{cases} \tag{14}$$

$v_f(t)$ is the Washburn-type flow velocity after the critical time t_c, and t_{max} is the time at which the horizontal fracture is fully saturated and all fluid is channeled further down into the vertical fracture segment.

Figure 5 shows the different flow stages observed in the SPH simulation, and Figure 7 shows the time-dependent penetration $l(t)$ and inflow velocity $dl(t)/dt$ obtained from Equation 14 for an aperture $a = 2.5$ mm and an inflow rate of $Q_0 = 4 \times 10^{-5}$ m^{2}s^{-1} to $Q_0 = 8 \times 10^{-5}$ m^{2}s^{-1}. The early time behavior is characterized by a plug-flow regime and hence $l(t) \sim t$, whereas after the critical time t_c, the inflow scales as $l(t) \sim \sqrt{t}$ (gray lines show both scaling regimes). At the time t_c, the analytical solution assumes a sudden jump in velocity due to the flow transitions from pure plug-flow within the horizontal fracture to a Washburn-type flow due to the breakthrough at the fracture intersection. The flow velocity in the horizontal fracture drops because of less fluid volume entering the fracture (which is instead channeled downwards onto the vertical fracture). The analytical solution for the penetration velocity dl/dt can describe both regimes (before and after the critical time t_c) and is in very good agreement with the numerical result. A slight deviation can be observed right after the onset of the Washburn behavior at time t_c, where channeling into the lower vertical fracture is initiated. Here, a very brief buildup of fluid at the fracture intersection occurs until a critical contact angle is reached and fluid flows downwards, that is, the breakthrough process is not perfectly instantaneous as assumed in the analytical solution but occurs over a small time window close to t_c. Figure 5 shows three partitioning types that have been determined based on a qualitative observation. For smaller t_c, the breakthrough process is a rather rapid process ("fast breakthrough" right column, Figure 5), while for larger t_c (and for example lower flow rates Q_0), the buildup of fluid on the vertical surface slightly disperses the breakthrough (Figure 5, left and middle column, "slow" and "moderately fast" breakthrough), yet a clear sequential progression of plug flow followed by Washburn flow in the horizontal fracture can be observed. The process of fluid buildup is not explicitly considered in our solution and is likely to induce the small temporary drop of the inflow velocity right after t_c (beyond the correct drop in velocity due to fluid entering the lower vertical surface instead of the horizontal fracture). However, at later times the velocity correctly converges toward the $l(t) \sim t^{0.5}$ scaling. The cutoff at t_{max} is not shown here because the simulations are stopped when flow reaches the end of the horizontal fracture such that $dl/dt = 0$. It should be noted that for very small t_c or large Q_0, flow may not exhibit the clear dynamics of sequential partition-

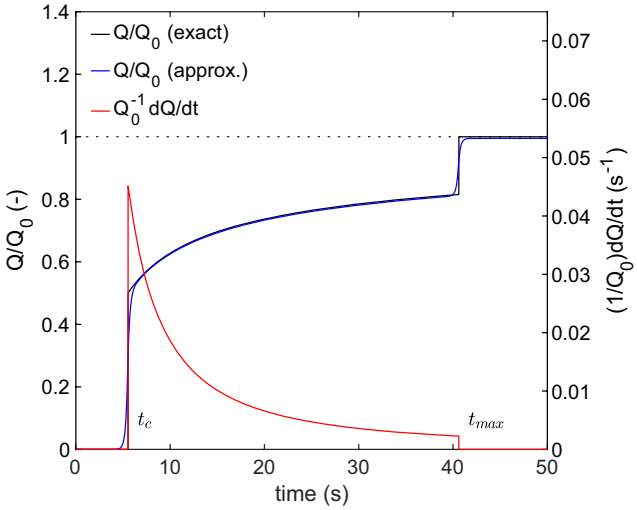

Figure 8. Normalized outflow rate and transfer function $\varphi(t) = Q_0^{-1}dQ\ /\ dt$ for a system with $a = 2.5$ mm and $Q_0 = 5 \times 10^{-5}$ m^2/s. The approximate solution for the outflow rate employs an replacement function for the Dirac function (Equation 19).

ing and a breakthrough can occur right away even before the theoretical time t_c due to effects of inertia, which we do not consider. Yet, for the covered range of flow rates, our model is in very good agreement with the theoretical solution.

To model the response of the system to a constant input signal Q_0, we obtain the outflow rate Q leaving the system:

$$Q = Q_0 - v_f(t)a. \tag{15}$$

Thus, the dimensionless flow rate is

$$F(t) = \frac{Q(t)}{Q_0} = H(t - t_c) - \frac{1}{2}\left(\frac{t}{t_c}\right)^{-1/2} \mathbb{I}(t_c < t < t_{max}). \tag{16}$$

Next, we define the normalized transfer function as

$$\varphi(t) = \frac{dF(t)}{dt}. \tag{17}$$

The transfer function for a plug-flow type regime followed by a Washburn-type behavior has the form

$$\begin{aligned}\varphi(t) = \frac{dF}{dt} = \delta(t - t_c) + \frac{1}{2}\left(\frac{t}{t_c}\right)^{-1/2}\left[\delta(t - t_{max}) - \delta(t - t_c)\right] \\ + \frac{1}{4t_c}\left(\frac{t}{t_c}\right)^{-3/2}, I(t_c < t < t_{max})\end{aligned} \tag{18}$$

where δ is the Dirac delta function.

To numerically integrate the transfer function, we replace the Dirac delta function in Equation 18 by

$$\delta \approx \delta_n(t) = \begin{cases} \frac{1}{\Delta t}, & -\frac{\Delta t}{2} < t < \frac{\Delta t}{2} \\ 0, & \text{otherwise} \end{cases} \tag{19}$$

where $\Delta t = 0.1$. Figure 8 shows the normalized outflow rate Q/Q_0 (exact and approximate solution) and its derivative, the normalized transfer function $\varphi = Q_0^{-1}dQ\,/\,dt$. The outflow Q/Q_0 is zero at first (all fluid is filling the horizontal fracture) until the critical time t_c, where partitioning sets in and inflow is characterized by a Washburn behavior. Finally, when the horizontal fracture is fully saturated at t_{max}, the outflow Q/Q_0 reaches its maximum value, that is, $Q = Q_0$ and $Q/Q_0 = 1$.

3.3. Extension of the Transfer Function

In the previous section, we focused on the process of horizontal fracture inflow and partitioning; however, we did not consider the effect of additional vertical surfaces above or below the fracture intersection, which affect the system response and therefore the transfer function. In the following section, we extend the transfer function based on classical Nusselt film flow approximations (Nusselt, 1916), which assume a constant film thickness.

The velocity profile of flow down an inclined plane in the x direction is governed by

$$\frac{d^2v_x}{dy^2} = -\frac{\rho g \sin(\alpha)}{\mu}, \tag{20}$$

where y is the direction normal to the surface and α is the inclination angle from the horizontal. The boundary conditions are established via a no-slip condition at $y = 0$, that is, $v_x(0) = 0$, and the normal viscous stress being zero at the free surface $y = h$,

$$\left.\frac{dv_x}{dy}\right|_{y=h} = 0. \tag{21}$$

The solution of this problem is

$$v_x(y) = \frac{\rho g \sin(\alpha)}{2\mu} y(2h - y). \tag{22}$$

The volumetric flux down the plane is then calculated as

$$Q = \int_0^h v_x dy = \frac{\rho g \sin(\alpha) h^3}{3\mu} \tag{23}$$

and, hence, the maximum film height for a given Q is

$$h = \left(\frac{3\mu Q}{\rho g \sin(\alpha)}\right)^{1/3}. \tag{24}$$

The depth-averaged velocity can be obtained as

$$\bar{v} = \frac{Q}{h} = \int_0^h v_x dy. \tag{25}$$

The effect of the upper vertical surfaces is simply a delay in the first arrival, i.e., a positive shift in the transfer function by Δt^v_{up}, given that $Q = Q_0$. Using Equation 25, we can then simply compute Δt^v_{up} as

$$\Delta t^v_{up} = L^v_{up} \frac{h}{Q_0} = \frac{L^v_{up}}{\bar{v}_{up}} \tag{26}$$

where L^v_{up} is the total length of the upper vertical surface. On the lower vertical surface, a similar shift in the transfer function is induced; however, here the outflow rate is initially $Q_c = Q(t_c)$. It should be noted that here t_c is the critical time since the beginning of the fracture penetration. For the sake of simplicity, we neglect the increase in Q after the breakthrough at t_c and assume that the flow velocity on the lower vertical surface depends on the breakthrough flow rate Q_c. The flow rate at the critical breakthrough is obtained via Equations 14 and 15 as

$$Q_c = Q_0 - v_c a, \tag{27}$$

where $v_c = \lim_{\epsilon \to 0} v_f(t = t_c + \epsilon)$. We then obtain the time Δt^v_{low} as

$$\Delta t^v_{low} = L^v_{low} \frac{h}{Q_c} = \frac{L^v_{low}}{\bar{v}_{low}} \tag{28}$$

and define the total shift induced by the upper and lower vertical surfaces as

$$\Delta T = \Delta t^v_{up} + \Delta t^v_{low}. \tag{29}$$

The cutoff at time t_{max}, when the horizontal fracture is fully saturated can be computed by setting $l(t_{max}) = l_{max}$, which gives

$$t_{max} = t_c (l_{max} / l_c)^2 \tag{30}$$

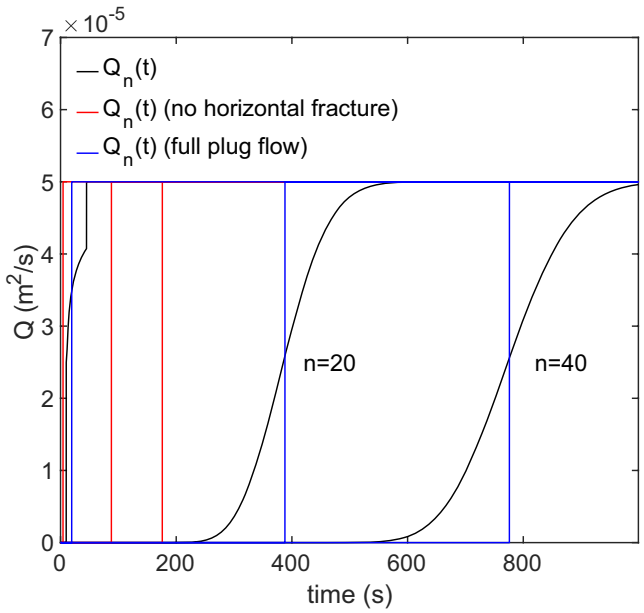

Figure 9. Application of the transfer function Equation 18 with Equation 19 and the convolution Equation 32 to a system of $n = 1$, 20, and 40 fractures and $L_{max} = 0.3$ m where $t_{max} > t_c$ (for further parameters, see section 3.4). The solution takes into account the shift in time of Δt^v_{up} and Δt^v_{low}. Simplified cases for $n = 1$, 20 and 40 neglect the impact of the horizontal fracture (red) or assume constant plug-flow until t_{max} (blue).

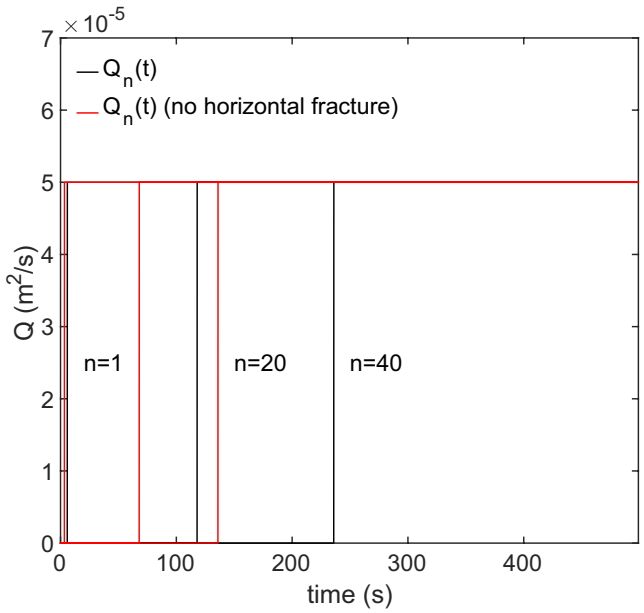

Figure 10. Application of the transfer function Equation 18 with Equation 19 and the convolution Equation 32 to a system of $n = 1$, 20, and 40 fractures and $L_{max} = 0.05$ m where $t_{max} < t_c$ (for further parameters, see section 3.4). The solution takes into account the shift in time of Δt^v_{up} and Δt^v_{low}. The simplified case for $n = 1$, 20, and 40 neglects the impact of the horizontal fracture (red).

The flow rate at the cutoff time t_{max} can be evaluated using Equation 14 with $v_{max}(t = t_{max} - \lim_{x\to\infty}\frac{1}{x})$ yielding the flow rate

$$Q_{max} = Q_0 - v_{max}a. \tag{31}$$

We are now able to compute the full transfer function, including the residence times on the upper and lower vertical surfaces as well as the cutoff at full fracture saturation. In the next chapter, we extend this analysis to model discharge through arbitrary large stacks of fracture intersections via linear response theory.

3.4. Analytical Percolation Model for Fracture Cascades

Following Noffz et al. (2019), we employ the transfer function in the context of linear response theory (Jury et al., 1986) to model the outflow rate $Q_n(t)$ at the bottom of the vertical surface intersected by n horizontal fractures. For the sake of comparison, two additional simplified cases are considered: (1) Flow within the horizontal fracture is governed entirely by plug-flow even when $t_{max} > t_c$, and (2) horizontal fractures are inactive due to missing capillary action (e.g., macropores, cave-like structures). The considered geometry and its properties with respect to the transformation of an input signal Q_0 serves as a proxy for consecutive routing through further fracture intersections of similar geometry. The outflow rate can be found as a convolution of the input signal

$$Q_n(t) = Q_0 \int_0^t dt_1 \varphi(t - t_1) \int_0^{t_1} dt_2 \varphi(t_1 - t_2) \cdots \int_0^{t_{n-1}} dt_n \varphi(t_n), \tag{32}$$

or

$$Q_n(t) = \int_0^t \varphi(t - t') Q_{n-1}(t') dt' \tag{33}$$

Note that for $n = 1$, the outflow rate $Q_1 = Q$ is given by Equation 15.

Figure 9 shows an example for the computed outflow rates $Q_n(t)$ for a system of $n = 1$, 25 and 50 fractures, employing Equation 32 and the transfer function Equation 18 where $t_{max} > t_c$ with the Dirac delta approximation Equation 19. Here, the maximum horizontal fracture length is $L_{max} = 0.3$ m, the aperture $a = 2.5$ mm, the static contact angle $\theta_0 = 69.0°$, the density $\rho = 1{,}000$ kgm^{-3}, the surface tension $\sigma = 0.0742$ kgs^{-2}, viscosity $\mu = 0.005$ kgm^{-1}s^{-1}, and the inflow rate $Q_0 = 5 \times 10^{-5}$ m^{2}s^{-1}. The upper and lower vertical surfaces have a length of $L^v_{up} = L^v_{low} = 0.2$ m. The two additional cases exhibit no dispersion because of missing Washburn-type dynamics. If the impact of horizontal fracture is completely ignored, the arrival times are nearly one order of magnitude lower than in the complex case. When the penetration is entirely governed by plug-flow, the first moments of the breakthrough correspond to the first moments of the complex case including Washburn-flow. However, the first arrival in the latter case occurs earlier due to the pressure-induced breakthrough.

Figure 10 shows the outflow rate for a system with $L_{max} = 0.05$ m, where flow is dominated by a plug-flow behavior and $t_{max} > t_c$. As expected, the mean breakthrough velocity is higher and the maximum outflow rate Q_0

is reached faster because of the stronger dispersive effect of deeper horizontal fractures. As in the previous example, a faster breakthrough is observed when horizontal fractures are ignored. However, due to the comparably small length of the horizontal fracture, the effect is less pronounced.

3.5. Arrival Times and Dispersion

The distribution of residence times after n horizontal fractures is defined by

$$f_n(t) = \frac{1}{Q_0}\frac{dQ_n(t)}{dt} = \int_0^t dt_1 \varphi(t-t_1)\int_0^{t_1} dt_2 \varphi(t_1-t_2)\cdots \int_0^{t_{n-2}} dt_{n-1}\varphi(t_{n-2}-t_{n-1})\varphi(t_{n-1}) \tag{34}$$

and its Laplace transform is given by

$$f_n^*(\lambda) = \varphi^*(\lambda)^n. \tag{35}$$

The first and second moments of the travel time are given by

$$m_j = (-1)^j \frac{d^j f_n^*(\lambda)}{d\lambda^j}\bigg|_{\lambda=0} \tag{36}$$

for $j = 1, 2$, or

$$m_1 = -n\varphi^*(\lambda)^{n-1}\frac{d\varphi^*(\lambda)}{d\lambda}\bigg|_{\lambda=0} \tag{37}$$

$$m_2 = n\varphi^*(\lambda)^{n-1}\frac{d^2\varphi^*(\lambda)}{d\lambda^2}\bigg|_{\lambda=0} + n(n-1)\varphi^*(\lambda)^{n-2}\left[\frac{d\varphi^*(\lambda)}{d\lambda}\right]^2\bigg|_{\lambda=0}. \tag{38}$$

Thus, for the mean and the variance of residence time we obtain

$$m_1 = -n\frac{d\varphi^*(\lambda)}{d\lambda}\bigg|_{\lambda=0} \quad \sigma^2 = n\frac{d^2\varphi^*(\lambda)}{d\lambda^2}\bigg|_{\lambda=0} - n\left[\frac{d\varphi^*(\lambda)}{d\lambda}\right]^2\bigg|_{\lambda=0}. \tag{39}$$

This means that the first moment and the variance are given by

$$m_1 = nh_1, \sigma^2 = n(h_2 - h_1^2), \tag{40}$$

where h_1 and h_2 are the first and second moments of the residence time for a single fracture. They are given by (see Appendix C)

$$h_1 = t_c\left(\frac{t_{max}}{t_c}\right)^{3/2} \tag{41}$$

$$h_2 = t_c^2\left[\frac{1}{3} + \left(\frac{t_{max}}{t_c}\right)^{3/2}\right]. \tag{42}$$

To determine the fluid arrival times after n fractures, we add a constant time shift ΔT to the residence time in a single horizontal fracture. Thus, the quantities h_1 and h_2 are modified as

$$h_{1T} = h_1 + \Delta T \tag{43}$$

$$h_{2T} = h_2 + 2h_1\Delta T + \Delta T^2. \tag{44}$$

We nondimensionalize time with respect to the critical time t_c such that

$$\tilde{h}_1 = \frac{h_1}{t_c} = \tau_m^{1/2} \tag{45}$$

$$\tilde{h}_2 = \frac{h_2}{t_c^2} = \frac{1}{3} + \frac{2}{3}\tau_m^{3/2}, \tag{46}$$

where $\tau_m = t_{\max}/t_c$ is found from Equation 30 as

$$\tau_m = (l_{max} \,/\, l_c)^2. \tag{47}$$

The arrival time moments are nondimensionalized accordingly as

$$\tilde{h}_{1T} = \tau_m^{1/2} + \tau_0 \tag{48}$$

$$\tilde{h}_{2T} = \frac{1}{3} + \frac{2}{3}\tau_m^{3/2} + 2\tau_m^{1/2}\tau_0 + \tau_0^2, \tag{49}$$

where the dimensionless $\tau_0 = \Delta T/t_c$ (Equations 12 and 29) is given by

$$\tau_0 = \frac{\Delta z}{2}\frac{[3\,\mu Q_0 \,/\, \rho g \sin(\alpha)]^{1/3} 6\,\mu Q_0}{a^3 \sigma \cos(\theta)}(1 + 2^{2/3}). \tag{50}$$

The equivalent flow velocity and dispersion coefficients are given in terms of the mean m_1 and variance σ^2 of the arrival times at a plane at $z = n\Delta z$, where Δz is the spacing between horizontal fractures,

$$v = \frac{n\Delta z}{m_1} \tag{51}$$

$$D = \frac{v^3\sigma^2}{2n\Delta z}. \tag{52}$$

We nondimensionalize lengths by Δz and obtain

$$\tilde{v} = \frac{1}{\tilde{h}_{1T}} = \frac{1}{\tau_m^{1/2} + \tau_0} \tag{53}$$

$$\tilde{D} = \frac{1}{2\tilde{h}_{1T}^3}\left(\tilde{h}_{2T} - \tilde{h}_{1T}^2\right) = \frac{\frac{1}{3} + \frac{2}{3}\tau_m^{3/2} - \tau_m}{2\left(\tau_m^{1/2} + \tau_0\right)^3}. \tag{54}$$

In the following, we study the behavior of the nondimensional dispersion coefficient $\tilde{D}$ and the flow velocity $\tilde{v}$ as functions of the nondimensional times τ_m and τ_0.

3.6. Dimensionless Analysis of Flow Through a Fracture Network

To investigate the effect of nondimensional times τ_m and τ_0 on the dimensionless flow velocity $\tilde{v}$ and dispersion coefficient $\tilde{D}$ (Equations 53 and 54), we conduct a multiparameter study. The minimum and maximum values of τ_m and τ_0 are computed for all parameter combinations of Q_0, $l_{\max}$, θ_0, a, and Δz. As we carry out our study in 2D, the proposed ranges for the flow rate should be interpreted in terms of the maximum film thick-

ness on the vertical surface. We vary Q_0 in the range of 1×10^{-6} to 1×10^{-2} m^2s^{-1}, which yields a film thickness on the vertical surfaces between 63.7 μm and 1.5 mm according to Equation 24. This range has been observed and modeled in various studies (Dragila & Weisbrod, 2003; Dragila & Wheatcraft, 2001; Patnaik & Perez-Blanco, 1996; Tokunaga & Wan, 1997). However, it should be noted that flows in the upper range on the order of millimeters are known to develop a wavy-laminar structure with low and high amplitude waves traveling as a rolling film (Ghezzehei, 2004; Patnaik & Perez-Blanco, 1996) and therefore are likely to deviate from the simple film flow approximation. The horizontal fracture depth l_{max} ranges from 0.01 to 4 m with an aperture a of 0.5–10 mm. The upper limit of the fracture length range has been chosen following Olson et al. (2007), who demonstrated that cumulative fracture lengths in fractured systems under various stress boundary conditions converge toward a maximum value of ∼4 m. While fracture apertures cover all length scales from micron to centimeter scales (Bonnet et al., 2001), apertures in the vadose zone are more likely to cover the upper portion of this range due to less overburden pressure and possibly enhanced dissolution (e.g., in karstic limestones). The chosen aperture range has for example been reported by Bahat (1987) and Weisbrod et al. (1998), who studied fractured chalk systems in the northern Negev desert of Israel. For apertures on the order of tens of millimeters, the assumption of capillary-driven flow in the horizontal fracture is likely violated in natural systems, and low-capillary free surface flows may develop. The static contact angle θ_0 is chosen to vary from 5° to 85° corresponding to a wetting regime that has been observed in various studies (Sobolev et al., 2000; Su et al., 1999, 2001; Tokunaga & Wan, 2001). Even lower or higher angles are possible, but this changes the conceptual framework. Near-zero contact angles may indicate spreading of a fluid, for example, because of micro-roughness or interaction with adsorbed films in the presence of a porous matrix (Shigorina et al., 2017; Tokunaga & Wan, 1997). Contact angles above 90° indicate hydrophobic conditions and fluids would require external forces beyond the capillary drag to enter a void space such as a fracture. The latter conditions are rarely met and have been observed in soil systems (Bachmann et al., 2000). Finally, the vertical fracture spacing Δz ranges from 0.1 to 25 m. For the sake of simplicity, we have chosen an equidistant setup for the vertical spacing, while natural fracture systems are often classified with respect to their regularity and follow a distribution (Hooker et al., 2013; Marrett et al., 2018). As we nondimensionalize the bulk properties with respect to the constant fracture spacing Δz, it is difficult to include a distribution in the analytical expressions derived here. However, in principle, the model can employ an irregular fracture spacing via suitable distributions in the transfer function φ and computation of the outflow (and dispersion) via Equation 32.

For the given parameter ranges, τ_m can take values between 8.1×10^{-6} and 1.4×10^{5} and τ_0 between 3.2×10^{-15} and 6.46. While the above chosen parameters are within feasible ranges, we further limit the relevant range of τ_m and τ_0 by constraining the Reynolds numbers within the horizontal fracture. Here we calculate the critical Reynolds numbers as

$$Re_c = \frac{\rho v_c a}{\mu} \tag{55}$$

where the characteristic velocity v_c is computed from the critical length and time

$$v_c = \frac{l_c}{t_c} \tag{56}$$

We chose a maximum value of $Re_c = 150$ to stay within the steady nonlinear laminar flow regime as that studied by Dybbs and Edwards (1984).

Figures 11 and 12 show the nondimensional dispersion $\tilde{D}$ and flow velocity $\tilde{v}$ plotted versus the dimensionless times τ_m and τ_0 over the entire chosen parameter space. The color-coded circles represent the critical Reynolds number Re_c for each parameter combination scaled from 0.1 to 150, where blue corresponds to lower values. Recall that τ_m encodes the timescale related to the imbibition process in the horizontal fractures, and τ_0 encodes the timescale for flow on the vertical fracture. Figure 11 (left) shows the dependence of the nondimensional dispersion coefficient $\tilde{D}$ on the horizontal fracture timescale τ_m for several values of the vertical fracture timescale τ_0. In general, $\tilde{D}$ increases with higher values of τ_m and approaches a constant maximum of $\tilde{D} = 0.08$ for $\tau_m > 10^5$. Within the maximum ranges defined for the Reynolds number, only

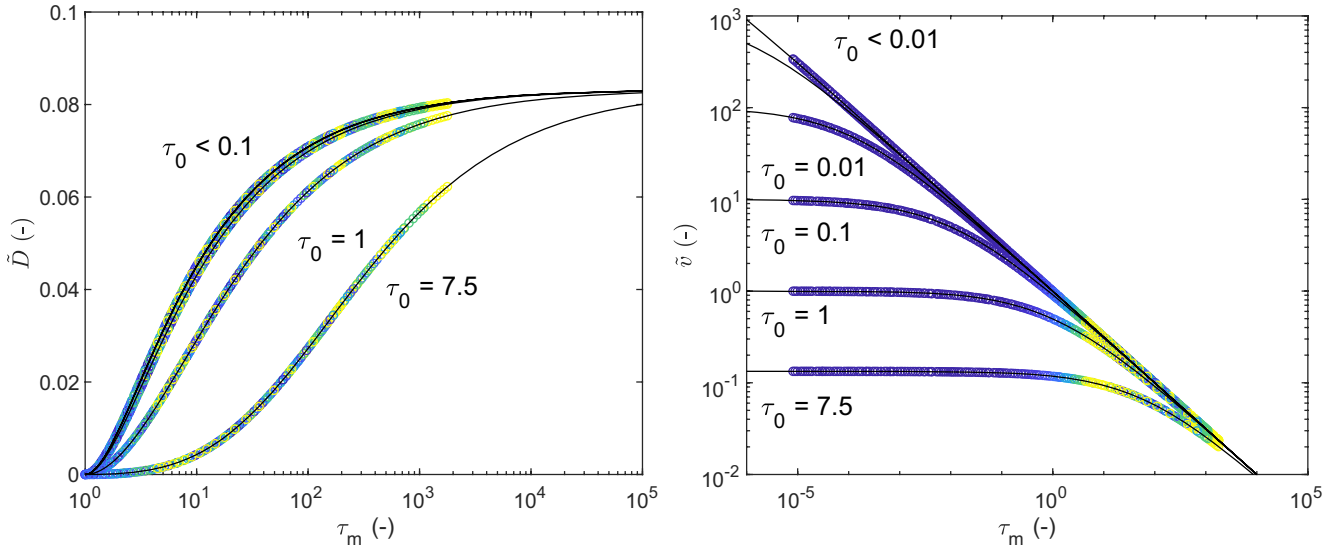

Figure 11. Nondimensional dispersion coefficient $\tilde{D}$ and flow velocity $\tilde{v}$ versus the dimensionless horizontal fracture timescale τ_m. Colored circles represent critical Reynolds numbers Re_c scaled from 0.1 (blue) to 150 (yellow). Note that $\tau_m \geq 1$ for the left plot because the strict analytical solution for the pure plug-flow regime ($t_{max} < t_c$, $t_{max}/t_c < 1$) does not cause any type of dispersion.

values of $\tau_0 < 1$ are close to reaching this constant maximum, while for $\tau_0 > 1$, the dispersion increases for the considered range of τ_m. The smaller initial gradient of $\Delta\tilde{D} / \Delta\tau_m$ (e.g., $\tau_0 = 7.5$) is caused by the nonlinear Washburn dynamics within the horizontal fracture. For smaller values of τ_m, the initial rapid (potentially plug-flow type when $t_{max} < t_c$) infiltration dominates the bulk flow, while for higher values of τ_m, the classical $\sqrt{t}$ scaling comes into effect and causes stronger dispersion of the breakthrough signal. Furthermore this example demonstrates how the ratio of τ_m and τ_0 affects the nondimensional dispersion coefficient. Increasing the ratio of τ_0/τ_m strengthens the dominance of the vertical flow paths and therefore decreases the overall dispersion, which in our model entirely stems from the horizontal fracture imbibition. However, it should be noted that this effect is negligible for values of $\tau_0 < 10^{-5}$ (Re_c restricted) and already vanishes for $\tau_0 < 0.1$. This is similar to the behavior displayed by the dimensional example (Figures 9 and 10), where the

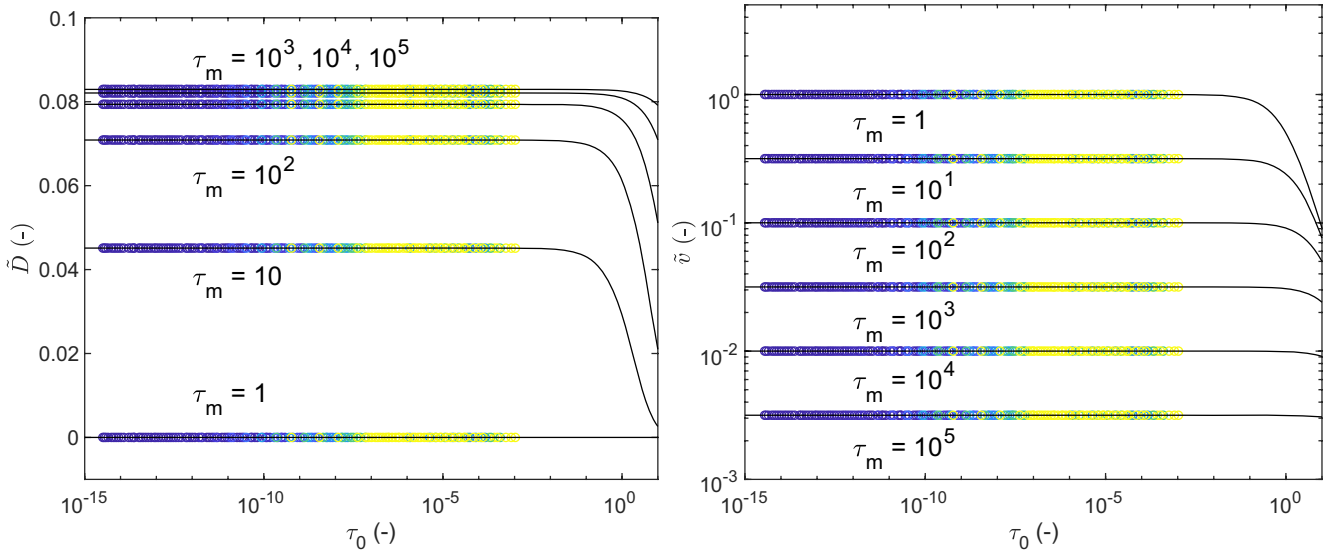

Figure 12. Nondimensional dispersion coefficient $\tilde{D}$ and flow velocity $\tilde{v}$ versus the dimensionless vertical fracture timescale τ_0. Colored circles represent critical Reynolds numbers Re_c scaled from 0.1 (blue) to 150 (yellow).

number of fractures and, therefore, the magnitude of horizontal imbibition (inversely related to the fracture spacing Δz) is positively correlated with the dispersion and for plug-flow-regime dynamics, no dispersion occurs ($t_{\max} > t_c$, equivalent to a very high ratio of τ_0/τ_m or low values of τ_m).

Figure 11 (right) demonstrates the dependence of the dimensionless flow velocity $\tilde{v}$ on the horizontal fracture timescale τ_m for a range of τ_0 between 0 and 7.5. Two regimes can be observed. For low values of τ_m, the velocity converges toward a constant value, while for higher τ_m, the nondimensional velocity scales as $\tilde{v} \sim \tau_m^{-1/2}$ in accordance with Equation 53. This transition occurs at the time τ_m that increases with τ_0/τ_m because of the increased impact of vertical film flow dynamics and plug-flow type dynamics in the horizontal fracture. For $\tau_0 \leq 0.01$ the velocity scales as $\tilde{v} \sim \tau_m^{-1/2}$ over nearly the entire range of feasible τ_m values, and the average breakthrough velocities decline with increasing magnitude of the horizontal fracture imbibition (e.g., deeper or wider fractures, higher static contact angles). For even lower values of $\tau_0 < 10^{-5}$ in the Re_c-restricted range, a perfect $\tilde{v} \sim \tau_m^{-1/2}$ scaling governs the functional relation between nondimensional velocity and horizontal fracture imbibition timescale, and no regime transition occurs.

Next, we discuss the dependence of $\tilde{D}$ and $\tilde{v}$ on the vertical fracture timescale τ_0. Figure 12 (left) demonstrates the limited influence of the vertical fracture timescale τ_0 on the nondimensional dispersion. Only for extreme end-members of the parameter range beyond $\tau_0 \approx 1$ is the effect of vertical fracture flow strong enough to counteract the dispersive action of the horizontal fracture and introduce a reduction in dispersion. However, within critical Re_c ranges, $\tilde{D}$ is only a function of τ_m. For values of $\tau_m > 10^3$ the relationship converges toward the constant value of $\tilde{D} \approx 0.08$.

Similarly, the nondimensional velocity is independent of the vertical fracture flow timescale τ_0 within critical Re_c ranges and is only dependent on the flow dynamics within the horizontal fracture encoded by τ_m with a $\tilde{v} \sim \tau_m^{-1/2}$ scaling behavior. It should be noted that this scaling holds for values of $\tau_m < 1$ (see Figure 11, right); however, here the nondimensional dispersion is $\tilde{D} = 0$ and flow is entirely governed by plug flow in the horizontal fracture and film flow on vertical surfaces.

4. Conclusion and Outlook

In this work, we developed an analytical solution for partially saturated flow through an arbitrarily large sugar-cube type fracture network consisting of wide-aperture horizontal fractures intersected by a vertical fracture. Based on numerical observations using an SPH code and former laboratory studies, we treat the partitioning dynamics at the fracture intersection as a sequential process whereby the fluid is channeled from the upper vertical surface into the horizontal fracture and finally onto the lower vertical fracture surface. Flow within the horizontal fracture is shown to follow plug-flow theory until critical pressure thresholds are exceeded. After the breakthrough, horizontal infiltration is governed by a Washburn-type scaling until the maximum horizontal fracture depth is reached and the outflow at the bottom of the system equals the inflow rate at the top. To model flow through arbitrarily large networks of the same internal structure, we capture this process with an analytical transfer function and carry out a convolution of the constant input signal following linear response theory. Given the complex parameter space of fluid and geometric properties, we analyze the outflow dynamics in terms of nondimensional values of τ_m and τ_0 that encode the timescales of flow in the horizontal and vertical fractures and relate them to the nondimensional dispersion coefficient $\tilde{D}$ and velocity $\tilde{v}$. It is shown that within the feasible Reynolds number range, the dimensionless dispersion coefficient converges to the value of $\tilde{D} \approx 0.08$ with increasing τ_m and is nearly independent of τ_0, that is, the flow in the vertical fracture does not have an impact on the dispersion coefficient. Furthermore, the bulk flow velocities are characterized by a $\tilde{v} \sim \tau_m^{-1/2}$ scaling that holds for all relevant values of τ_m and is independent of τ_0 within critical Re_c ranges.

Our work demonstrates the importance of horizontal fractures as drivers for the (lateral) dispersive action within a mainly vertically oriented flow field. This conclusion clearly deviates from the classical piston-flow dynamics that are often assumed in the field(continuum)-scale flow models in fractured-porous systems (Arbel et al., 2010; Lange et al., 2010). As demonstrated in this work, neglecting the effects of Washburn-type dynamics (i.e., assuming pure piston flow) and/or neglecting the impact of horizontal fractures heavily alters the dispersive bulk properties and decreases (mean) breakthrough times. Furthermore, our work sheds

light on the relation between integral signals at outlet boundaries (e.g., water table fluctuations within boreholes) and the internal system geometry that transforms input signals (precipitation, recharge) and mainly contributes to the dispersion and bulk velocity within the vadose zone.

In our analysis, we simplify the infiltration process in terms of the fracture-network geometry as well as the partitioning process and flow mode occurrence. Our study assumes film flow on all vertical surfaces. This assumption is often made in studies related to preferential flow in soil systems and the respective macropore structure (Bogner & Germann, 2019; Germann et al., 2007; Nimmo, 2010, 2012; Nimmo & Perkins, 2018). However, other flow modes such as flow-rate-dependent droplets (slugs) and rivulets are likely to occur on fracture surfaces (Dippenaar & Van Rooy, 2016; Dragila & Weisbrod, 2003, 2004; Ghezzehei & Or, 2005; Jones et al., 2017) and are known to affect partitioning at intersections (Kordilla et al., 2017; T. R. Wood et al., 2005; Xue et al., 2020). While droplets are more likely to bypass intersections due to their extended height (as compared to films) and hence gravitational impact (Kordilla et al., 2017), we have also demonstrated that consecutive routing of droplet flows through arrays of horizontal fractures will nearly always facilitate the formation of film (rivulet) flows on the vertical wide-aperture surfaces after the first partitioning (Noffz et al., 2019). Subsequently, flow is mostly channeled into horizontal fractures without bypass, supporting the assumption of sequential flow dynamics made in this study.

Because our study is limited to a two-dimensional fracture network, the observed dependence of the non-dimensional dispersion $\tilde{D}$ and velocity $\tilde{v}$ on the vertical and horizontal fracture flow timescales must be interpreted with care. For stable infiltration fronts, the infiltration dynamics of three-dimensional systems can be accurately recovered with two-dimensional models (e.g., Kordilla et al., 2017) using homogenization over the third dimension. However, flow on vertical fracture surfaces tends to develop instabilities even when these surfaces are perfectly smooth (Shigorina et al., 2019). Such front instabilities can contribute to fracture-specific channeling and additional dispersion. Front instabilities can develop in horizontal fractures as well, even though the formation of instabilities here is not caused by gravitational pull but is mainly a result of viscous forces and velocity variations due to changes in fracture aperture (roughness) and variations of the capillary radius (Nicholl & Glass, 2005). Apart from the dimensionality of the system, the geometrical properties such as the inclinations of the horizontal and vertical fractures are clearly simplified because natural systems often deviate from the classical "sugar-cube" geometry. Nonhorizontal fractures will decrease the breakthrough time t_c when inclination angles are positive (relative to the horizontal) due to additional gravitational drag on the fluid entering the fracture. Negative inclination angles may not only increase the breakthrough times (due to increasing drag on the fluid front into the fracture) but may even lead to a complete change in the conceptual model if fluid leaves the horizontal fractures when reaching the maximum depth $l_{\max}$. For horizontal fractures and under wetting conditions, this effect does not occur even when the fracture is open at $l_{\max}$. The conceptual base for such processes would require adding a sink term to the transfer function and therefore increasing the bulk dispersion. Such effects are important when assessing flow convergence and integrative properties of fracture networks (Glass & LaViolette, 2004; LaViolette et al., 2003) within the vadose zone and add another level of complexity to the problem at hand.

In contrast to other studies, we focus on the case of vertical fractures with wide apertures. Here, the term "wide" should be interpreted with respect to the probability of fluid wetting opposing sites of the vertical fracture. For contact angles in the range of 25° to 75° droplet heights (neglecting the dynamic flattening due to movement) would be on the order of 0.75–2.4 mm, therefore setting a lower limit where one-sided flow would persist. Studies focusing on "narrow" vertical fractures often observe a slightly wider range of partitioning patterns that stem from the erratic uptake and emittance of potentially chaotic droplet patterns from T-type (Xue et al., 2020; Yang et al., 2019) and X-type intersections (e.g., Glass et al., 2003; T. R. Wood et al., 2005; T. Wood & Huang, 2015). While the majority of fractures under common geological conditions will belong to the "narrow" category, wide-aperture fractures are more likely to be found in the vadose zone where overburden pressure is limited and especially in karstic environments where fractures can be affected by dissolution (Dahan et al., 1999, 2000). Because most studies are still focusing on individual intersections dynamics, a unified theory for a broad range of apertures and partitioning dynamics is still to be developed.

Upscaling of individual processes, such as the intersection uptake and partitioning dynamics, remains one of the most challenging aspects in the current state of infiltration dynamics in fractured-porous media. In this work, we demonstrated how to bridge the gap between small-scale process and larger-scale

bulk application using a simple convolution and the analytical derivation of (nondimensional) dispersion and velocity parameters. In its current form, the model assumes that convolution occurs over an arbitrary number of equally structured intersections. In principle, this could be extended to sequences of intersections with dynamic properties by introducing parameter distributions that reflect changes in the transfer function φ and therefore outflow $Q_n(t)$ over the range of encountered fractures n (Equation 32). However, while this would enhance the applicability to natural geological systems, analytical forms of $\tilde{D}$ and $\tilde{v}$ would be more difficult to derive. Inclusion of more complex partitioning of different flow mode dynamics, (e.g., droplets; Xue et al., 2020; Yang et al., 2019) would be an interesting, yet highly challenging extension because the uptake and release of such flows at intersections introduces a highly erratic and chaotic component.

As our model assumes impermeable fracture walls, we cannot model effects of porous matrix storage. This is justified for low-permeable porous systems, such as granites, or impermeable limestone surfaces. When considering the porous matrix, both the vertical fracture walls as well as the horizontal walls will retard the movement within the fracture (e.g., Buscheck et al., 1991) and could be introduced via suitable storage (sink) terms into the transfer function. The potential influence of the matrix imbibition depends on the consolidated material. Sandstones are typically at the upper end of the porosity and permeability (sorptivity) range and are considered for the following brief example. Assuming a porosity of $\theta = 0.2$ and sorptivity of $S = 0.15$ cm s$^{-0.5}$ (e.g., Berea sandstone, Kang et al., 2013), a first-order approximation for the potential fluid uptake in the studied examples can be made. For the sake of simplicity, we assume that fluid imbibes into the porous matrix in the horizontal direction across the entire length of the upper vertical fractures $L^v_{up} = 0.2$ m and neglects potential imbibition normal to the horizontal fracture plane during the penetration. For $Q_0 = 3 \times 10^{-5}$ m^2.s^{-1}, an aperture of $a = 2.5$ mm, critical time $t_c = 17$ s, and length $l_c = 0.2$ m (see Figure 4) yields a horizontal imbibition depth of $l_{imb} = S\sqrt{t_c} = 0.61$ cm and therefore a fluid volume of $A^m = \theta l_{imb} L^v_{up} = 2.44 \times 10^{-4}$ m^2. The volume stored within the fracture until t_c is $A^f = a l_c = 5 \times 10^{-4}$ m^2. Therefore the imbibition into the matrix could potentially reduce the inflow volume and hence velocity during this time period by about 50%.

To derive consistent and process-based infiltration functions for fractured-porous media, it is crucial to unify the various observed patterns for partitioning dynamics across the scientific community. This will require further studies at laboratory and field scales to elucidate the shortcomings of each approach and obtain a suitable array of methods adjusted for the respective study setting and data availability. Given the strong impacts of climate-change-induced transformation of precipitation patterns (Black, 2009), water resources management, specifically in arid and semi-arid regions, requires enhanced models for recharge prediction that take into account the rapid preferential flow component that may substantially contribute to groundwater replenishment under high evapotranspiration and short but extreme rainfall conditions (Pachauri et al., 2014).

Appendix A: Smoothed Particle Hydrodynamics Model

We employ the SPH method to model free surface flow of water described by the Navier-Stokes (NS) equations, including the momentum and conservation equations

$$\frac{d\mathbf{v}}{dt} = -\frac{\nabla P}{\rho} + \frac{\mu}{\rho}\nabla^2\mathbf{v} + \mathbf{g} \qquad \nabla \cdot \mathbf{v} = 0, \tag{A1}$$

respectively, subject to the Young boundary condition at the liquid–gas–solid interface, the Young-Laplace boundary condition at the water–air interface and the no-slip boundary condition at the liquid–solid interface (Kordilla et al., 2017; Tartakovsky & Meakin, 2005a; Tartakovsky & Panchenko, 2016). Here, $\mathbf{v}$ is the velocity, P is the pressure, ρ is the density, μ is the viscosity, and $\mathbf{g}$ is the gravitational acceleration.

To simplify the solution of the incompressible NS Equation A1, we employ the weakly compressible formulation where the continuity equation is replaced with its compressible form $d\rho/dt = -\rho\nabla \cdot \mathbf{v}$, and the equation of state is used to close the resulting compressible NS equations:

$$P(\rho) = c_0^2 \frac{\rho_0}{7}\left(\left[\frac{\rho}{\rho_0}\right]^7 - 1\right) + P_0, \tag{A2}$$

where ρ_0 is the reference water density and P_0 is a background pressure. The speed of sound c_0 is chosen such that $|\delta\rho|/\rho \leq 0.03$, where $|\delta\rho|$ is the maximum absolute change in density. This condition is sufficient for fluid to behave as an incompressible fluid and to obtain an accurate pressure field (Morris et al., 1997).

The SPH discretization of the weakly compressible NS equation is:

$$\begin{aligned}\frac{d\mathbf{v}_i}{dt} = &\sum_{j\in s+f} m_j\left(\frac{P_i}{\rho_i^2} + \frac{P_j}{\rho_j^2}\right)\hat{\mathbf{e}}_{ij}\frac{\partial W(\mathbf{r}_{ij},h)}{\partial r_{ij}} + \sum_{j\in f} m_j \frac{\mu_i + \mu_j}{\rho_i\rho_j}\frac{\mathbf{v}_{ij}}{r_{ij}}\frac{\partial W(\mathbf{r}_{ij},h)}{\partial r_{ij}} \\ &+ \sum_{j\in s+f}\frac{1}{m_j}\mathbf{F}_{ij}^I + \sum_{k\in s}\mathbf{F}_{ik}^B + \mathbf{g},\end{aligned} \tag{A3}$$

and

$$\frac{d\rho_i}{dt} = \sum_{j=1}^{N} m_j \mathbf{v}_{ij}\cdot\hat{\mathbf{e}}_{ij}\frac{\partial W(\mathbf{r}_{ij},h)}{\partial r_{ij}}, \tag{A4}$$

where $\hat{\mathbf{e}}_{ij} = \mathbf{r}_{ij}/r_{ij}$ is the unit vector pointing from particle i to particle j, summations are over all fluid (f) and/or solid (s) particles, and W is a two-dimensional Wendland kernel (Wendland, 1995) that establishes a smoothed interaction over the range h between particles. To simulate surface tension an additional pairwise interaction term (Tartakovsky & Meakin, 2005a) is employed that consists of two overlapping cubic spline functions W_1 and W_2 with a short-range repulsive and long-range attractive component controlled by coefficients A and B (Kordilla et al., 2013, 2017):

$$\mathbf{F}_{ij}^I = s\left[AW_1(r_{ij},h_1) - BW_2(r_{ij},h_2)\right]\hat{\mathbf{e}}_{ij}. \tag{A5}$$

The magnitude of the interaction force depends on the factor s, which assumes values of s_{sf} for solid–fluid interactions and s_{ff} for fluid–fluid interactions. For values of $s_{sf} > s_{ff}$, wetting conditions are enforced, while otherwise nonwetting fluids can be simulated.

No-slip conditions are enforced via a Robin-type volumetric force term following Pan et al. (2014)

$$\mathbf{F}_{ik}^B = \beta\mathbf{v}_i\frac{m_k}{\rho_i\rho_k}(\mathbf{n}_i + \mathbf{n}_k)\cdot\hat{\mathbf{e}}_{ij}\frac{\partial W(\mathbf{r}_{ik},h)}{\partial r_{ik}} \tag{A6}$$

where $\mathbf{n}_i$ is the normal unit vector (see the definition in Pan et al. (2014), $\beta = \mu/\lambda$ is the friction coefficient, and λ is the artificial slip length. For most fluids, the real slip length is on the order of several nanometers, and using such a small λ would result in a prohibitively small time step in the SPH method. We demonstrate in Section 2.1 that the no-slip boundary condition can be accurately modeled by setting λ to be 100 times smaller than the domain size. We note that in Equation A3, the summation of the viscosity term is only over fluid particles, while the no-slip condition is entirely enforced via Equation A6.

The highly nonlinear form of the equation A2 generates sufficiently high pressure (in addition to the repulsive part of the interaction force) to prevent fluid particles from penetrating solid surfaces.

To integrate Equation A3, a modified Velocity Verlet time-stepping scheme is employed and time steps are constrained as follows (Kordilla et al., 2017; Pan et al., 2014; Tartakovsky & Meakin, 2005c):

$$\Delta t \leq \delta\frac{h}{c}, \qquad \Delta t \leq \delta\min\sqrt{h/|\mathbf{a}_i|}, \qquad \Delta t \leq \delta\min\frac{\rho_i h^2}{\mu_i}, \qquad \Delta t \leq \delta\min\frac{h(\rho_i+\rho_j)}{2\beta} \tag{A7}$$

where $\delta = 0.1$.

Appendix B: Spontaneous Imbibition

The volumetric flow rate through a fracture conceptualized as a parallel plate is governed by:

$$\frac{dV}{dt} = \frac{\Delta P}{\Delta l}\frac{a^3}{12\mu}W, \tag{B1}$$

where l is the penetration depth (the length over which the pressure gradient ΔP acts), a is the aperture and W is the fracture (unit) width. The change in volume over time can be rewritten in terms of the penetration depth into the fracture

$$\frac{dV}{dt} = aW\frac{dl}{dt} \tag{B2}$$

Plugging this into Equation B1, we obtain

$$\frac{dl}{dt} = \frac{\Delta P}{\Delta l}\frac{a^2}{12\mu} \tag{B3}$$

The capillary pressure according to Young's law in the case of a parallel plate is

$$\Delta P_c^{2D} = \frac{\sigma\cos(\theta_0)}{r}, \tag{B4}$$

where r is the radius of the fracture. Here, we neglect the second principal radius which would otherwise, in the case of a tube geometry for example, yield

$$\Delta P_c^{3D} = \sigma\cos(\theta_0)\left(\frac{1}{r_1}+\frac{1}{r_2}\right) \tag{B5}$$

Plugging this into Equation B3, we obtain

$$\frac{dl}{dt} = \frac{\sigma\cos(\theta_0)a^2}{rl(t)12\ \mu} = \frac{\sigma\cos(\theta_0)(2r)^2}{rl(t)12\ \mu} = \frac{\sigma\cos(\theta_0)r}{l(t)3\ \mu} \tag{B6}$$

Separating the variables and integration from l_c to $l(t)$ on the left and from t_c to t on the right side yields

$$\int_{l(t_0)}^{l} l(t)dl = \int_{t_0}^{t}\frac{\sigma\cos(\theta_0)r}{3\ \mu}dt \tag{B7}$$

and

$$\frac{1}{2}l(t)^2 = \frac{\sigma cos(\theta_0)r}{3\ \mu}t + C \tag{B8}$$

such that the time-dependent penetration length becomes

$$l(t) = \left(\frac{2\sigma cos(\theta_0)r}{3\ \mu}(t-t_c)+l_c^2\right)^{1/2} \tag{B9}$$

Note that this Washburn-type flow behavior is only valid at times much larger than t_c. We do not model the transitional flow between the plug and Washburn modes, but represent the change between the two modes as abrupt and match the linear and square root behaviors at time t_c.

Appendix C: Moments

To calculate the moments of $\varphi(t)$, it is advantageous to write the equation as follows,

$$\begin{aligned}\varphi(t) &= \frac{dF}{dt} = \delta(t-t_c) + W(t)\Big[\delta(t-t_{max}) - \delta(t-t_c)\Big] \\ &-W'(t)\mathbb{I}(t_c < t < t_{max})\end{aligned} \tag{C1}$$

where we set

$$W = \frac{1}{2}\left(\frac{t}{t_c}\right)^{-1/2} \tag{C2}$$

$$W' = -\frac{1}{4t_c}\left(\frac{t}{t_c}\right)^{-3/2} \tag{C3}$$

The zeroth moment is

$$\int_0^\infty dt\varphi(t) = 1 + [W(t_{max}) - W(t_c)] - [W(t_{max}) - W(t_c)] = 1. \tag{C4}$$

Now we determine the first moment:

$$\int_0^\infty dtt\varphi(t) = t_c + [t_{max}W(t_{max}) - t_cW(t_c)] + \frac{\sqrt{t_c}}{4}\int_{t_c}^{t_{max}} dtt^{-1/2} \tag{C5}$$

$$= t_c + [t_{max}W(t_{max}) - t_cW(t_c)] + \frac{\sqrt{t_c}}{2}(\sqrt{t_{max}} - \sqrt{t_c}) \tag{C6}$$

$$= t_c\sqrt{t_{max}\ /\ t_c} \tag{C7}$$

Now we determine the second moment:

$$\int_0^\infty dtt^2\varphi(t) = t_c^2 + [t_{max}^2W(t_{max}) - t_c^2W(t_c)] + \frac{\sqrt{t_c}}{4}\int_{t_c}^{t_{max}} dtt^{1/2} \tag{C8}$$

$$= t_c^2 + [t_{max}^2W(t_{max}) - t_c^2W(t_c)] + \frac{\sqrt{t_c}}{6}(t_{max}^{3/2} - t_c^{3/2}) \tag{C9}$$

$$= t_c^2\left[\frac{1}{3} + \frac{2}{3}(t_{max}\ /\ t_c)^{3/2}\right] \tag{C10}$$

Data Availability Statement

All experimental data can be downloaded from https://data.goettingen-research-online.de/dataset.xhtml?persistentId=doi:10.25625/77DVJA

References

Adler, P. M., Thovert, J. F., & Mourzenko, V. V. (2013). Fractured porous media (Vol. 9780199666). Oxford University Press. https://doi.org/10.1093/acprof:oso/9780199666515.001.0001

Alkhatib, J., Engelhardt, I., Ribbe, L., & Sauter, M. (2019). An integrated approach for choosing suitable pumping strategies for a semi-arid region in Jordan using a groundwater model coupled with analytical hierarchy techniques. *Hydrogeology Journal*, *27*(4), 1143–1157. https://doi.org/10.1007/s10040-019-01925-0 Retrieved from http://link.springer.com/10.1007/s10040-019-01925-0

Acknowledgments
J. Kordilla acknowledges support by the Open Access Publication Funds of the Göttingen University and funding from the German Research foundation (grant no. KO 5359/1-1). M. Dentz gratefully acknowledges funding from the Spanish Ministry of Science and Innovation through the project HydroPore (grant no: PID2019-106887GB-C31). A. Tartakovsky was supported by the U.S. Department of Energy (DOE) Office of Science, Office of Advanced Scientific Computing Research as part of the New Dimension Reduction Methods and Scalable Algorithms for Nonlinear Phenomena project. Open access funding enabled and organized by Projekt DEAL.

Arbel, Y., Greenbaum, N., Lange, J., & Inbar, M. (2010). Infiltration processes and flow rates in developed karst vadose zone using tracers in cave drips. *Earth Surface Processes and Landforms*, *35*(14), 1682–1693. https://doi.org/10.1002/esp.2010

Ascott, M. J., Gooddy, D. C., Wang, L., Stuart, M. E., Lewis, M. A., Ward, R. S., & Binley, A. M. (2017). Global patterns of nitrate storage in the vadose zone. *Nature Communications*, *8*(1), 1–6. http://dx.doi.org/10.1038/s41467-017-01321-w

Ascott, M. J., Wang, L., Stuart, M. E., Ward, R. S., & Hart, A. (2016). Quantification of nitrate storage in the vadose (unsaturated) zone: A missing component of terrestrial N budgets. *Hydrological Processes*, *30*(12), 1903–1915. https://doi.org/10.1002/hyp.10748

Bachmann, J., Horton, R., van der Ploeg, R. R., & Woche, S. (2000). Modified sessile drop method for assessing initial soil-water contact angle of sandy soil. *Soil Science Society of America Journal*, *64*(2), 564–567. https://doi.org/10.2136/sssaj2000.642564x

Bahat, D. (1987). Jointing and fracture interactions in middle eocene chalks near beer sheva, Israel. *Tectonophysics*, *136*(3–4), 299–321. https://doi.org/10.1016/0040-1951(87)90031-X

Barenblatt, G. I., Zheltov, I. P., & Kochina, I. N. (1960). Basic concepts in the theory of seepage of homogeneous liquids in fissured rocks [strata]. *Journal of Applied Mathematics and Mechanics*, *24*(5), 1286–1303. https://doi.org/10.1016/0021-8928(60)90107-6

Barozzi, G. S., & Angeli, D. (2014). A note on capillary rise in tubes. *Energy Procedia*, *45*, 548–557. https://doi.org/10.1016/j.egypro.2014.01.059

Benson, D. A. (2001). A model of water streaking down a wall. *Water Resources Research*, *37*(2), 427–430. https://doi.org/10.1029/2000WR900309

Berkowitz, B., & Scher, H. (1995). On characterization of anomalous dispersion in porous and fractured media. *Water Resources Research*, *31*(6), 1461–1466. http://doi.wiley.com/10.1029/95WR00483

Black, E. (2009). The impact of climate change on daily precipitation statistics in Jordan and Israel. *Atmospheric Science Letters*, *10*(3), 192–200. https://doi.org/10.1002/asl.233

Bodvarsson, G., Bandurraga, T., & Wu, Y. (1997). *The site-scale unsaturated zone model of Yucca Mountain, Nevada, for the viability assessment, Yucca Mountain characterization project report LBNL-40376, UC-814 (Tech. Rep.)*. Berkeley, CA: Earth Sciences Division, Lawrence Berkeley National Laboratory.

Bogner, C., & Germann, P. (2019). Viscous flow approach to "pushing out old water" from undisturbed and repacked soil columns. *Vadose Zone Journal*, *18*(1), 1–10. https://doi.org/10.2136/vzj2018.09.0168

Bonnet, E., Bour, O., Odling, N. E., Davy, P., Main, I., Cowie, P., & Berkowitz, B. (2001). Scaling of fracture systems in geological media. *Reviews of Geophysics*, *39*(3), 347–383. https://doi.org/10.1029/1999RG000074

Buscheck, T. A., Nitao, J. J., & Chesnut, D. A. (1991). The impact of episodic nonequilibrium fracture-matrix flow on repository performance at the potential Yucca Mountain site. *MRS Proceedings*, *257*. https://doi.org/10.1557/proc-257-607

Chambers, L. A., Gooddy, D. C., & Binley, A. M. (2019). Use and application of CFC-11, CFC-12, CFC-113 and SF6 as environmental tracers of groundwater residence time: A review. *Geoscience Frontiers*, *10*(5), 1643–1652. https://doi.org/10.1016/j.gsf.2018.02.017

Cook, P. G., & Solomon, D. K. (1997). Recent advances in dating young groundwater: Chlorofluorocarbons, 3H/3He and 85Kr. *Journal of Hydrology*, *191*(1–4), 245–265. https://doi.org/10.1016/S0022-1694(96)03051-X

Dahan, O., Nativ, R., Adar, E. M., Berkowitz, B., & Ronen, Z. (1999). Field observation of flow in a fracture intersecting unsaturated chalk. *Water Resources Research*, *35*(11), 3315–3326. https://doi.org/10.1029/1999WR900198

Dahan, O., Nativ, R., Adar, E. M., Berkowitz, B., & Weisbrod, N. (2000). On fracture structure and preferential flow in unsaturated chalk. *Ground Water*, *38*(3), 444–451.

Dijk, P. E., Berkowitz, B., & Yechieli, Y. (2002). Measurement and analysis of dissolution patterns in rock fractures. *Water Resources Research*, *38*(2), 51–512. http://doi.wiley.com/10.1029/2001WR000246

Dippenaar, M. A., & Van Rooy, J. L. (2016). On the cubic law and variably saturated flow through discrete open rough-walled discontinuities. *International Journal of Rock Mechanics and Mining Sciences*, *89*, 200–211. https://doi.org/10.1016/j.ijrmms.2016.09.011

Dragila, M. I., & Weisbrod, N. (2003). Parameters affecting maximum fluid transport in large aperture fractures. *Advances in Water Resources*, *26*(12), 1219–1228. https://doi.org/10.1016/j.advwatres.2003.09.002

Dragila, M. I., & Weisbrod, N. (2004). Fluid motion through an unsaturated fracture junction. *Water Resources Research*, *40*(2), 1–11. https://doi.org/10.1029/2003WR002588

Dragila, M. I., & Wheatcraft, S. (2001). Free surface films. In *Conceptual models of flow and transport in the fractured vadose zone* (pp. 217–241). National Academies Press.

Dvory, N. Z., Livshitz, Y., Kuznetsov, M., Adar, E., & Yakirevich, A. (2016). The effect of hydrogeological conditions on variability and dynamic of groundwater recharge in a carbonate aquifer at local scale. *Journal of Hydrology*, *535*, 480–494. http://dx.doi.org/10.1016/j.jhydrol.2016.02.011

Dybbs, A., & Edwards, R. (1984). A new look at porous media fluid mechanics–Darcy to turbulent. In *Fundamentals of transport phenomena in porous media* (pp. 199–256). Springer.

Ebel, B. A., & Nimmo, J. R. (2013). An alternative process model of preferential contaminant travel times in the unsaturated zone: Application to Rainier Mesa and Shoshone Mountain, Nevada. *Environmental Modeling & Assessment*, *18*(3), 345–363. https://doi.org/10.1007/s10666-012-9349-8

El-Hakim, M., & Bakalowicz, M. (2007). Significance and origin of very large regulating power of some karst aquifers in the Middle East. Implication on karst aquifer classification. *Journal of Hydrology*, *333*(2–4), 329–339. Retrieved from https://linkinghub.elsevier.com/retrieve/pii/S0022169406004768, https://doi.org/10.1016/j.jhydrol.2006.09.003

Engelhardt, I., Rausch, R., Lang, U., Al-Saud, M., & Schüth, C. (2013). Impact of Preboreal to Subatlantic shifts in climate on groundwater resources on the Arabian Peninsula. *Environmental Earth Sciences*, *69*(2), 557–570. https://doi.org/10.1007/s12665-013-2362-7

Flint, A. L., Flint, L. E., Bodvarsson, G. S., Kwicklis, E. M., & Fabryka-Martin, J. (2001). Development of the conceptual model of unsaturated zone hydrology at Yucca Mountain, Nevada. *Journal of Hydrology*, *247*, 47–85. https://doi.org/10.1016/S0022-1694(01)00358-4

Ford, D., & Williams, P. (2013). *Karst hydrogeology and geomorphology*. John Wiley \& Sons. https://doi.org/10.1002/9781118684986

Germann, P. F., Helbling, A., & Vadilonga, T. (2007). Rivulet Approach to Rates of Preferential Infiltration. *Vadose Zone Journal*, *6*(2), 207. https://doi.org/10.2136/vzj2006.0115 Retrieved from https://www.soils.org/publications/vzj/abstracts/6/2/207

Germann, P. F., & Hensel, D. (2006). Poiseuille Flow Geometry Inferred from Velocities of Wetting Fronts in Soils. *Vadose Zone Journal*, *5*(3), 867. https://doi.org/10.2136/vzj2005.0080 Retrieved from https://www.soils.org/publications/vzj/abstracts/5/3/867

Ghezzehei, T. A. (2004). Constraints for flow regimes on smooth fracture surfaces. *Water Resources Research*, *40*(11). https://doi.org/10.1029/2004WR003164

Ghezzehei, T. A., & Or, D. (2005). Liquid fragmentation and intermittent flow regimes in unsaturated fractured media. *Water Resources Research*, *41*(12), 1–10. https://doi.org/10.1029/2004WR003834

Glass, R. J., & LaViolette, R. A. (2004). Self-organized spatial-temporal structure within the fractured Vadose Zone: Influence of fracture intersections. *Geophysical Research Letters*, *31*(15), 1–4. https://doi.org/10.1029/2004GL019511

Glass, R. J., Nicholl, M. J., Rajaram, H., & Wood, T. R. (2003). Unsaturated flow through fracture networks: Evolution of liquid phase structure, dynamics, and the critical importance of fracture intersections. *Water Resources Research*, *39*(12), 1–12. https://doi.org/10.1029/2003WR002015

Gunn, J. (1981). Limestone solution rates and processes in the Waitomo District, New Zealand. *Earth Surface Processes and Landforms*, *6*(5), 427–445. https://doi.org/10.1002/esp.3290060504

Hayden, K. M., Telyakovskiy, A. S., & Wheatcraft, S. W. (2012). A note on free-surface films in fractures. *Advances in Water Resources*, *49*, 72–75. https://doi.org/10.1016/j.advwatres.2012.06.012

Heppner, C. S., Nimmo, J. R., Folmar, G. J., Gburek, W. J., & Risser, D. W. (2007). Multiple-methods investigation of recharge at a humid-region fractured rock site, Pennsylvania, USA. *Hydrogeology Journal*, *15*(5), 915–927. https://doi.org/10.1007/s10040-006-0149-6

Hooker, J. N., Laubach, S. E., & Marrett, R. (2013). Fracture-aperture sized frequency, spatial distribution, and growth processes in strata-bounded and non-strata-bounded fractures, cambrian mesón group, NW Argentina. *Journal of Structural Geology*, *54*, 54–71. https://doi.org/10.1016/j.jsg.2013.06.011

Huang, H., Meakin, P., & Liu, M. (2005). Computer simulation of two-phase immiscible fluid motion in unsaturated complex fractures using a volume of fluid method. *Water Resources Research*, *41*(12), 1–12. https://doi.org/10.1029/2005WR004204

Hussain, S. I., Frey, S. K., Blowes, D. W., Ptacek, C. J., Wilson, D., Mayer, K. U., et al. (2019). Reactive transport of manure-derived nitrogen in the vadose zone: Consideration of macropore connectivity to subsurface receptors. *Vadose Zone Journal*, *18*(1), 2–18. https://doi.org/10.2136/vzj2019.01.0002

Jarvis, N. (1998). Modeling the impact of preferential flow on nonpoint source pollution. In H. Selim, & L. Ma (Eds.), *Physical nonequilibrium in soils: Modeling and application* (pp. 195–221). Ann Arbor Press Chelsea.

Ji, S. H., Nicholl, M. J., Glass, R. J., & Lee, K. K. (2004). Influence of a simple fracture intersection on density-driven immiscible flow: Wetting vs. nonwetting flows. *Geophysical Research Letters*, *31*(14), 10–13. https://doi.org/10.1029/2004GL020045

Ji, S.-H., Nicholl, M. J., Glass, R. J., & Lee, K.-K. (2006). Influence of simple fracture intersections with differing aperture on density-driven immiscible flow: Wetting versus nonwetting flows. *Water Resources Research*, *42*(10), 1–10. http://doi.wiley.com/10.1029/2006WR004953

Jones, B. R., Brouwers, L. B., Van Tonder, W. D., & Dippenaar, M. A. (2017). Assessing geotechnical centrifuge modelling in addressing variably saturated flow in soil and fractured rock. *Environmental Science and Pollution Research*, *24*(15), 13203–13223. https://doi.org/10.1007/s11356-016-8333-2

Jurin, J. (1718). An account of some experiments shown before the Royal Society; with an enquiry into the cause of some of the ascent and suspension of water in capillary tubes. *Philosophical Transactions of the Royal Society of London*, *30*, 739–747.

Jury, W. A., Sposito, G., & White, R. E. (1986). A Transfer function model of solute transport through soil: 1. Fundamental concepts. *Water Resources Research*, *22*(2), 243–247. http://doi.wiley.com/10.1029/WR022i002p00243

Kang, M., Perfect, E., Cheng, C., Bilheux, H., Gragg, M., Wright, D., et al. (2013). Diffusivity and sorptivity of Berea sandstone determined using neutron radiography. *Vadose Zone Journal*, *12*(3). https://doi.org/10.2136/vzj2012.0135

Kordilla, J., Noffz, T., Dentz, M., Geyer, T., & Tartakovsky, A. M. (2017). Effect of unsaturated flow modes on partitioning dynamics of gravity-driven flow at a simple fracture intersection: laboratory study and three-dimensional smoothed particle hydrodynamics simulations. *Water Resources Research*, *53*(11), 9496–9518. https://doi.org/10.1002/2016WR020236

Kordilla, J., Sauter, M., Reimann, T., & Geyer, T. (2012). Simulation of saturated and unsaturated flow in karst systems at catchment scale using a double continuum approach. *Hydrology and Earth System Sciences*, *16*(10), 3909–3923. https://doi.org/10.5194/hess-16-3909-2012

Kordilla, J., Tartakovsky, A. M., & Geyer, T. (2013). Advances in Water Resources A smoothed particle hydrodynamics model for droplet and film flow on smooth and rough fracture surfaces. *Advances in Water Resources*, *59*, 1–14. http://dx.doi.org/10.1016/j.advwatres.2013.04.009

Kurtzman, D., Shapira, R. H., Bar-Tal, A., Fine, P., & Russo, D. (2013). Nitrate fluxes to groundwater under citrus orchards in a Mediterranean climate: Observations, calibrated models, simulations and agro-hydrological conclusions. *Journal of Contaminant Hydrology*, *151*(3), 93–104. http://dx.doi.org/10.1016/j.jconhyd.2013.05.004

Lange, J., Arbel, Y., Grodek, T., & Greenbaum, N. (2010). Water percolation process studies in a Mediterranean karst area. *Hydrological Processes*, *24*(13), 1866–1879. https://doi.org/10.1002/hyp.7624

LaViolette, R. A., Glass, R. J., Wood, T. R., McJunkin, T. R., Noah, K. S., Podgorney, R. K., et al. (2003). Convergent flow observed in a laboratory-scale unsaturated fracture system[1]. *Geophysical Research Letters*, *30*(2), 10–12. http://doi.wiley.com/10.1029/2002GL015775

Legait, B., & de Gennes, P.-G. (1984). Capillary rise between closely spaced plates : effect of Van der Waals forces. *Journal de Physique Lettres*, *45*(13), 647–652. https://doi.org/10.1051/jphyslet:019840045013064700

Liu, H. H., Salve, R., Wang, J. S., Bodvarsson, G. S., & Hudson, D. (2004). Field investigation into unsaturated flow and transport in a fault: Model analyses. *Journal of Contaminant Hydrology*, *74*(1–4), 39–59. https://doi.org/10.1016/j.jconhyd.2004.02.004

Liu, M., Meakin, P., & Huang, H. (2007). Dissipative particle dynamics simulation of multiphase fluid flow in microchannels and microchannel networks. *Physics of Fluids*, *19*(3), 1–11. https://doi.org/10.1063/1.2717182

Marrett, R., Gale, J. F., Gómez, L. A., & Laubach, S. E. (2018). Correlation analysis of fracture arrangement in space. *Journal of Structural Geology*, *108*, 16–33. https://doi.org/10.1016/j.jsg.2017.06.012

Morris, J., Fox, P. J., & Zhu, Y. (1997). Modeling low {Reynolds} number incompressible flows using {SPH}. *Journal of Computational Physics*, *136*(1), 214–226. https://doi.org/10.1006/jcph.1997.5776

Neslon, R. (2001). *Geologic analysis of naturally fractured reservoirs*. Elsevier. https://doi.org/10.1016/b978-0-88415-317-7.x5000-3

Nicholl, M. J., & Glass, R. J. (2005). Infiltration into an Analog Fracture. *Vadose Zone Journal*, *4*(4), 1123. https://doi.org/10.2136/vzj2004.0110 Retrieved from https://www.soils.org/publications/vzj/abstracts/4/4/1123

Nimmo, J. R. (2010). Theory for source-responsive and free-surface film modeling of unsaturated flow. *Vadose Zone Journal*, *9*(2), 295. https://doi.org/10.2136/vzj2009.0085

Nimmo, J. R. (2012). Preferential flow occurs in unsaturated conditions. *Hydrological Processes*, *26*(5), 786–789. https://doi.org/10.1002/hyp.8380

Nimmo, J. R., & Perkins, K. S. (2018). Episodic master recession evaluation of groundwater and streamflow hydrographs for water-resource estimation. *Vadose Zone Journal*, *17*(1), 180050. https://doi.org/10.2136/vzj2018.03.0050

Noffz, T., Dentz, M., & Kordilla, J. (2019). Analogue fracture experiments and analytical modeling of unsaturated percolation dynamics in fracture cascades. *Vadose Zone Journal*, *18*(1), 1–9. https://doi.org/10.2136/vzj2018.08.0155 Retrieved from https://onlinelibrary.wiley.com/doi/abs/10.2136/vzj2018.08.0155

Nusselt, W. (1916). Die Oberflächenkondensation des Wasserdampfes. *VDI-Zeitschriften*, *60*(27).

Olson, J. E., Laubach, S. E., & Lander, R. H. (2007). Combining diagenesis and mechanics to quantify fracture aperture distributions and fracture pattern permeability. *Geological Society, London, Special Publications*, *270*(1), 101–116. https://doi.org/10.1144/GSL.SP.2007.270.01.08 Retrieved from http://sp.lyellcollection.org/lookup/doi/10.1144/GSL.SP.2007.270.01.08

Pachauri, R. K., Allen, M. R., Barros, V. R., Broome, J., Cramer, W., Christ, R., et al. (2014). *Climate change 2014: Synthesis report. Contribution of working groups I, II and III to the fifth assessment report of the intergovernmental panel on climate change*. Cambridge, UK: Cambridge University Press.

Pan, W., Bao, J., & Tartakovsky, A. M. (2014). Smoothed particle hydrodynamics continuous boundary force method for Navier-Stokes equations subject to a Robin boundary condition. *Journal of Computational Physics*, *259*, 242–259. https://doi.org/10.1016/j.jcp.2013.12.014

Patnaik, V., & Perez-Blanco, H. (1996). Roll waves in falling films: An approximate treatment of the velocity field. *International Journal of Heat and Fluid Flow*, *17*(1), 63–70. https://doi.org/10.1016/0142-727X(95)00075-2

Popescu, M. N., Ralston, J., & Sedev, R. (2008). Capillary rise with velocity-dependent dynamic contact angle. *Langmuir*, *24*, 12710–12716. https://doi.org/10.1021/la801753t

Pratt, V. (1987). Direct least-squares fitting of algebraic surfaces. In Proceedings of the 14th annual conference on computer graphics and interactive techniques—Siggraph (87, pp. 145–152). New York, NY: ACM Press. https://doi.org/10.1145/37401.37420 Retrieved from http://portal.acm.org/citation.cfm?doid=37401.37420

Rossman, N. R., Zlotnik, V. A., Rowe, C. M., & Szilagyi, J. (2014). Vadose zone lag time and potential 21st century climate change effects on spatially distributed groundwater recharge in the semi-arid Nebraska Sand Hills. *Journal of Hydrology*, *519*(PA), 656–669. http://dx.doi.org/10.1016/j.jhydrol.2014.07.057

Sauter, M. (1992). Quantification and forecasting of regional groundwater flow and transport in a Karst Aquifer (Gallusquelle, Malm, SW. Germany) (Dissertation, 13). Tübingen: Eberhard Karls University of Tübingen.

Scanlon, B. R., & Cook, P. G. (2002). Theme issue on groundwater recharge. *Hydrogeology Journal*, *10*(1), 3–4. https://doi.org/10.1007/s10040-001-0175-3

Scanlon, B. R., Keese, K. E., Flint, A. L., Flint, L. E., Gaye, C. B., Edmunds, W. M., & Simmers, I. (2006). Global synthesis of groundwater recharge in semiarid and arid regions. *Hydrological Processes*, *20*(15), 3335–3370. https://doi.org/10.1002/hyp.6335

Shigorina, E., Kordilla, J., & Tartakovsky, A. M. (2017). Smoothed particle hydrodynamics study of the roughness effect on contact angle and droplet flow. *Physical Review E*, *96*(3), 033115. https://doi.org/10.1103/PhysRevE.96.033115 Retrieved from https://link.aps.org/doi/10.1103/PhysRevE.96.033115

Shigorina, E., Tartakovsky, A. M., & Kordilla, J. (2019). Investigation of gravity-driven infiltration instabilities in smooth and rough fractures using a pairwise-force smoothed particle hydrodynamics model. *Vadose Zone Journal*, *18*(1). https://doi.org/10.2136/vzj2018.08.0159

Sigalotti, L., Klapp, J., Sira, E., Melean, Y., & Hasmy, A. (2003). SPH simulations of time-dependent Poiseuille flow at low Reynolds numbers. *Journal of Computational Physics*, *191*(2), 622–638. https://doi.org/10.1016/S0021-9991(03)00343-7

Singhal, B., & Gupta, R. (2010). *Applied hydrogeology of fractured rocks*. Springer Science & Business Media.

Sobolev, V. D., Churaev, N. V., Velarde, M. G., & Zorin, Z. M. (2000). Surface tension and dynamic contact angle of water in thin quartz capillaries. *Journal of Colloid and Interface Science*, *222*(1), 51–54. https://doi.org/10.1006/jcis.1999.6597

Su, G. W., Geller, J. T., Pruess, K., & Hunt, J. R. (2001). Solute transport along preferential flow paths in unsaturated fractures. *Water Resources Research*, *37*(10), 2481–2491. https://doi.org/10.1029/2000WR000093

Su, G. W., Geller, J. T., Pruess, K., & Wen, F. (1999). Experimental studies of water seepage and intermittent flow in unsaturated, rough-walled fractures. *Water Resources Research*, *35*(4), 1019–1037. https://doi.org/10.1029/1998WR900127

Tartakovsky, A. M., & Meakin, P. (2005a). Modeling of surface tension and contact angles with smoothed particle hydrodynamics. *Physical Review E - Statistical, Nonlinear and Soft Matter Physics*, *72*(2), 1–9. https://doi.org/10.1103/PhysRevE.72.026301

Tartakovsky, A. M., & Meakin, P. (2005b). Simulation of Unsaturated Flow in Complex Fractures Using Smoothed Particle Hydrodynamics. *Vadose Zone Journal*, *4*(3), 848. https://doi.org/10.2136/vzj2004.0178 Retrieved from https://www.soils.org/publications/vzj/abstracts/4/3/0848

Tartakovsky, A. M., & Meakin, P. (2005c). A smoothed particle hydrodynamics model for miscible flow in three-dimensional fractures and the two-dimensional Rayleigh-Taylor instability. *Journal of Computational Physics*, *207*(2), 610–624. https://doi.org/10.1016/j.jcp.2005.02.001

Tartakovsky, A. M., & Panchenko, A. (2016). Pairwise Force Smoothed Particle Hydrodynamics model for multiphase flow: Surface tension and contact line dynamics. *Journal of Computational Physics*, *305*, 1119–1146. http://dx.doi.org/10.1016/j.jcp.2015.08.037

Tokunaga, T. K. (2009). *Hydraulic properties of adsorbed water films in unsaturated porous media*. eScholarship University of California.

Tokunaga, T. K., & Wan, J. M. (1997). Water Film Flow Along Fracture Surfaces of Porous \t\t\t Rock. *Water Resources Research*, *33*(6), 1287–1295. https://doi.org/10.1029/97wr00473 Retrieved from http://www.agu.org/journals/wr/v033/i006/97WR00473/97WR00473.pdf

Tokunaga, T. K., & Wan, J. M. (2001). Surface-zone flow along unsaturated rock fractures. *Water Resources Research*, *37*(2), 287–296. https://doi.org/10.1029/2000WR900242

Tsang, C.-F., Neretnieks, I., & Tsang, Y. (2015). Hydrologic issues associated with nuclear waste repositories. *Water Resources Research*, *51*(9), 6923–6972. http://doi.wiley.com/10.1002/2015WR017641

Wang, L., Butcher, A. S., Stuart, M. E., Gooddy, D. C., & Bloomfield, J. P. (2013). The nitrate time bomb: A numerical way to investigate nitrate storage and lag time in the unsaturated zone. *Environmental Geochemistry and Health*, *35*(5), 667–681. https://doi.org/10.1007/s10653-013-9550-y

Weisbrod, N., Nativ, R., Adar, E. M., & Ronen, D. (2000). Salt accumulation and flushing in unsaturated fractures in an arid environment. *Ground Water*, *38*(3), 452.

Weisbrod, N., Nativ, R., Ronen, D., & Adar, E. (1998). On the variability of fracture surfaces in unsaturated chalk. *Water Resources Research*, *34*(8), 1881–1887. https://doi.org/10.1029/98WR01447

Wendland, H. (1995). Piecewise polynomial, positive definite and compactly supported radial functions of minimal degree. *Advances in Computational Mathematics*, *4*(1), 389–396. https://doi.org/10.1007/BF02123482

Williams, P. W. (2008). The role of the epikarst in karst and cave hydrogeology: A review. *International Journal of Speleology*, *37*(1), 1–10. https://doi.org/10.5038/1827-806X.37.1.1

Wood, T., & Huang, H. (2015). Experimental and modeling studies of episodic air-water two-phase flow in fractures and fracture networks. In B. Faybishenko, S. M. Benson, & J. E. Gale (Eds.), *Fluid dynamics in complex fractured-porous systems* (pp. 209–228). Wiley.

Wood, T. R., Nicholl, M. J., & Glass, R. J. (2002). Fracture intersections as integrators for unsaturated flow. *Geophysical Research Letters*, *29*(24), 441–444. http://doi.wiley.com/10.1029/2002GL015551

Wood, T. R., Nicholl, M. J., & Glass, R. J. (2005). Influence of fracture intersections under unsaturated, low-flow conditions. *Water Resources Research*, *41*(4), 1–17. https://doi.org/10.1029/2004WR003281

Xue, S., Yang, Z., Hu, R., & Chen, Y. (2020). Splitting dynamics of liquid slugs at a T junction. *Water Resources Research*, *56*(8), 1–17. https://doi.org/10.1029/2020wr027730

Yang, Z., Xue, S., Zheng, X., & Chen, Y. (2019). Partitioning dynamics of gravity driven unsaturated flow through simple T shaped fracture intersections. *Water Resources Research*, *55*(8), 7130–7142. Retrieved from https://onlinelibrary.wiley.com/doi/abs/10.1029/2018WR024349, https://doi.org/10.1029/2018WR024349

Zhou, Q., Salve, R., Liu, H. H., Wang, J. S., & Hudson, D. (2006). Analysis of a mesoscale infiltration and water seepage test in unsaturated fractured rock: Spatial variabilities and discrete fracture patterns. *Journal of Contaminant Hydrology*, *87*(1–2), 96–122. https://doi.org/10.1016/j.jconhyd.2006.05.001